Energy Materials and Devices

Open Access
Review

Graphical Abstract

Advanced design strategies for cathode materials of nonaqueous aluminum-ion batteries

Liangjie Gu[1], Ming Lei[1], and Panpan Dong[1,2] ✉

[1] *Key Laboratory of Advanced Technologies of Materials (Ministry of Education), School of Materials Science and Engineering, Southwest Jiaotong University, Chengdu 610031, China*
[2] *Research Institute of Frontier Science, Southwest Jiaotong University, Chengdu 610031, China*

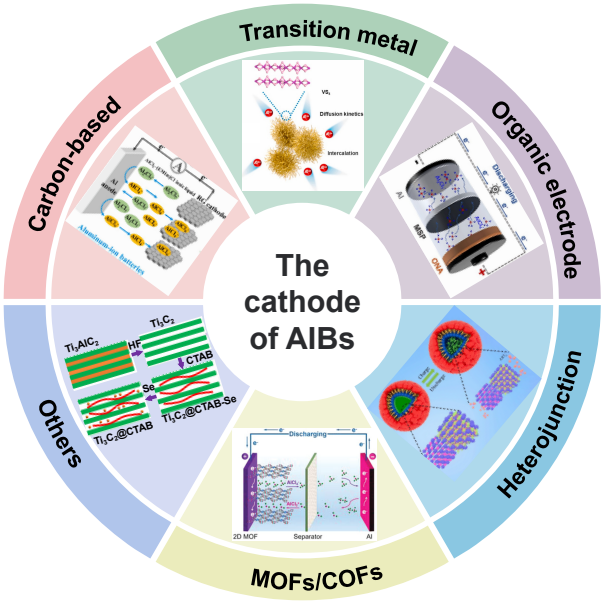

Nonaqueous aluminum-ion batteries (AIBs) have emerged as a promising alternative to lithium-ion systems for next-generation energy storage owing to their high theoretical capacity and inherent safety as well as the exceptional abundance of aluminum. However, the practical development of AIBs is primarily constrained by the performance limitations of the cathode materials, including low reversible capacity, inadequate cycling stability, and sluggish reaction kinetics. This review comprehensively examines approaches for designing the structure and optimizing the performance of cathode materials for nonaqueous AIBs and provides an outlook on prospective applications.

✉ Address correspondence to
Panpan Dong,
panpan.dong@swjtu.edu.cn

Received: January 16, 2026
Revised: March 3, 2026
Accepted: March 9, 2026

9370090

Read Online

Citation: Gu L., Lei M., Dong P. Advanced design strategies for cathode materials of nonaqueous aluminum-ion batteries. *Energy Mater. Devices*, 2026, 4(x), 9370090. https://doi.org/10.26599/EMD.2026.9370090

Energy Materials and Devices
https://doi.org/10.26599/EMD.2026.9370090
Open Access
Review

Advanced design strategies for cathode materials of nonaqueous aluminum-ion batteries

Liangjie Gu[1], Ming Lei[1], and Panpan Dong[1,2] ✉

[1] *Key Laboratory of Advanced Technologies of Materials* (*Ministry of Education*), *School of Materials Science and Engineering*, *Southwest Jiaotong University*, *Chengdu 610031*, *China*
[2] *Research Institute of Frontier Science*, *Southwest Jiaotong University*, *Chengdu 610031*, *China*

Cite this article: *Energy Mater. Devices* 2026, **4**(x): 9370090. https://doi.org/10.26599/EMD.2026.9370090

ABSTRACT

Nonaqueous aluminum-ion batteries (AIBs) are emerging as a viable postlithium energy-storage technology, leveraging the high theoretical capacity, safety, and elemental abundance of aluminum. However, the practical implementation of AIBs is predominantly hindered by the limited electrochemical performance of the cathode materials. This review provides a comprehensive and systematic analysis of recent advances in cathode materials for nonaqueous AIBs. We first elucidate the fundamental aluminum-storage mechanisms and then critically assess the progress across various material classes, including carbon-based architectures, transition-metal chalcogenides and oxides, organic compounds, engineered heterojunctions, and metal–organic/covalent organic frameworks and their derivatives. The discussion focuses on the intricate structure–property relationships governing key electrochemical metrics such as the capacity, cyclability, and rate performance. Finally, we highlight the persistent scientific and technical challenges within the field and propose strategic research directions for the rational design of next-generation, high-performance cathodes. This review offers critical insights and valuable guidance for the future development of practical nonaqueous AIBs systems.

KEYWORDS

nonaqueous, aluminum-ion batteries, cathode design, energy-storage mechanism

1 Introduction

Energy-storage technologies are of paramount importance for sustainable development[1–3]. Although lithium-ion batteries (LIBs) currently dominate the energy-storage market because of their exceptional performance, pressing issues such as resource scarcity (e.g., limited lithium and cobalt reserves), safety hazards (e.g., thermal runaway), and escalating costs have become increasingly prominent[4]. These challenges have spurred intensive research into alternative energy-storage systems, leading to the development of numerous emerging technologies, including sodium-ion[5–7], magnesium-ion[8,9], potassium-ion[10,11], zinc-ion[12,13], and aluminum-ion batteries (AIBs)[14–17]. Among these candidates, AIBs have emerged as a highly promising next-generation energy-storage technology, attributed to their ultrahigh theoretical specific capacity (804 mAh g^{-1} for the Al metal anode), abundant and low-cost aluminum resources (accounting for ~8% of the earth's crust), excellent safety performance (no risk of dendrite growth), and inherent cost-competitiveness[18–20]. AIBs are generally divided into aqueous and nonaqueous. Aqueous AIBs have gained considerable attention and undergone rapid development owing to their safety and environmental friendliness. The introduction of aluminum-alloy anodes and organic cathodes has improved the cycling stability of aqueous AIBs. Nevertheless, compared to their nonaqueous counterparts, the cycling performance, electrochemical stability window, and rate capability of aqueous AIBs remain inferior[21–24]. Nonaqueous AIBs employing tetrachloroaluminate ions ($AlCl_4^-$) as charge carriers have garnered significant research attention owing to their high practical energy density and more stable electrochemical performance compared to those of their aqueous counterparts[25–27].

However, the industrialization of nonaqueous AIBs is hindered by several critical technical bottlenecks, primarily centered on the cathode materials. Key challenges include sluggish ion-transport kinetics, low practical specific capacity, poor cycling stability, and irreversible damage to battery components caused by highly corrosive electrolytes (e.g., $AlCl_3$/ionic-liquid mixtures)[28,29]. For instance, the intercalation/deintercalation of $AlCl_4^-$ ions into/from the lattice of cathode materials during charge–discharge cycles is kinetically constrained, resulting in slow charging rates, low energy conversion efficiency, and inadequate rate capability, which severely limit the practical application of AIBs[30]. Therefore, the develop-

Received: January 16, 2026 / **Revised:** March 3, 2026 / **Accepted:** March 9, 2026

✉**Address correspondence to** Panpan Dong, panpan.dong@swjtu.edu.cn

ment of cathode materials that integrate high specific capacity, excellent rate performance, and long-term cycling stability has become the core focus and critical breakthrough point in current research regarding nonaqueous AIBs. To address these issues, researchers have explored a range of cathode types for nonaqueous AIBs, spanning carbon-based, transition-metal sulfide and oxide, organic, and heterojunction cathodes as well as cathodes comprising metal–organic/covalent organic frameworks (MOFs/COFs) and their derivatives, along with other materials. To better understand the development and history of cathode materials for nonaqueous AIBs, the timeline of important breakthroughs in this field is shown in Fig. 1. In 2015, Dai and co-workers[31] pioneered the use of graphite as a cathode material for nonaqueous AIBs, utilizing a chloroaluminate ionic liquid, $AlCl_3$/1-ethyl-3-methylimidazolium chloride ([EMIm]Cl) = 1.3:1 by mole, as the electrolyte. This landmark study demonstrated extraordinary and ultrafast charge–discharge capability of nonaqueous AIBs, delivering a high power density of 3000 W kg^{-1} alongside an exceptional cycling lifespan exceeding 7,500 cycles. This breakthrough has since catalyzed a surge in research interest, inspiring exploration of diverse cathode architectures to further enhance the electrochemical performance of nonaqueous AIBs[32–40].

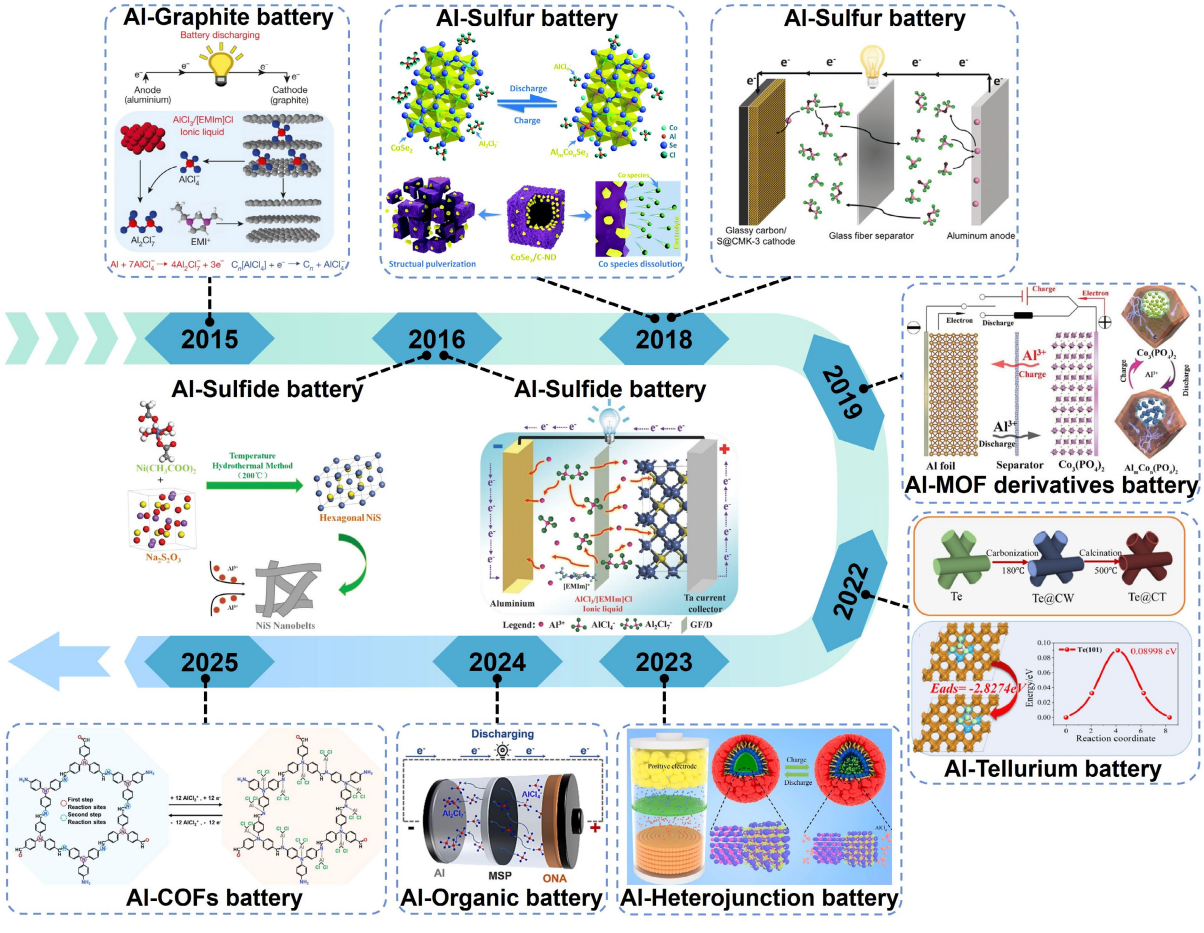

Figure 1 Timeline of cathode design for nonaqueous AIBs. The first use of graphite as a cathode material in nonaqueous AIBs. Schematic of Al/graphite cell during discharge using the optimal composition of the $AlCl_3$/1-ethyl-3-methylimidazolium chloride ($AlCl_3$/[EMIm]Cl) ionic-liquid electrolyte. Reproduced with permission from Ref. [31] ©2015, Springer Nature Limited. Schematic of fabrication of NiS nanobelts. Reproduced with permission from Ref. [32] ©2016, The Royal Society of Chemistry. First report of Ni_3S_2/graphene microsheet composite as a novel cathode material for rechargeable AIBs. Reproduced with permission from Ref. [33] ©2016, WILEY-VCH Verlag GmbH & Co. KGaA, Weinheim. Discharge process in Al-S battery with *N*-butyl-*N*-methylpiperidinium bromide/$AlCl_3$ (NBMPBr/$AlCl_3$) electrolyte. Reproduced with permission from Ref. [34] ©2018, Wiley-VCH Verlag GmbH & Co. KGaA, Weinheim. Schematic of proposed energy-storage and capacity-degradation mechanisms of $CoSe_2$-based cathode. Reproduced with permission from Ref. [35] ©2018, The Royal Society of Chemistry. Diagram of Al^{3+} insertion/extraction in Al-MOF battery during charging and discharging, highlighting the dual role of the carbon shell in enhancing structural stability and facilitating electron transport. Reproduced with permission from Ref. [36] ©2019, WILEY-VCH Verlag GmbH & Co. KGaA, Weinheim. Schematic of preparation of hollow nanotube carbon-coated tellurium, and diffusion paths and diffusion barriers of $AlCl_4^-$ in Te (101). Reproduced with permission from Ref. [37] ©2021, Elsevier Ltd. Reaction mechanism of Cu_2Se@MnSe heterojunction spherical shells. Reproduced with permission from Ref. [38] ©2023, Elsevier B.V. Diagram of the working mechanism of Al-oligomeric naphthalene (ONA) battery. Reproduced with permission from Ref. [39] ©2024, Elsevier B.V. Schematic of charge/discharge mechanism of triphenylamine (TPA)-COFs in AIBs. Reproduced with permission from Ref. [40] ©2025, Elsevier B.V.

The primary focus of this review is nonaqueous AIBs systems. A systematic summary of the latest research progress regarding mainstream cathode materials and in-depth insights into the aluminum-storage mechanisms of these materials are presented, including anion ($AlCl_4^-$) intercalation/de-intercalation, cation (Al^{3+} or $AlCl_2^+$) storage, and redox reactions coupled with multi-step synergistic processes. We discuss several key technical challenges currently facing nonaqueous AIBs and summarize effective strategies for enhancing their electrochemical performance, including morphology control (e.g., construction of nanostructured or hollow architectures), surface engineering (e.g., coating with protective layers), doping techniques (e.g., heteroatom doping to modulate the electronic structure), fabrication of composite electrodes (e.g., combining active materials with conductive substrates), and manipulation of charge-storage mechanisms (e.g., intercalation, conversion, or alloying reactions of materials with different structures). Finally, based on the current state of research, we identify the key scientific issues and technical challenges to be addressed and propose future research directions, aiming to provide valuable guidance for the rational design and development of high-performance cathode materials for nonaqueous AIBs.

2 Classification of materials, methods, and design of cathode materials

The charge-storage mechanism is a critical factor governing the key characteristics of cathode materials, including the specific capacity, redox potential, rate capability, and cycling stability, which significantly influence the electrochemical performance of nonaqueous AIBs[41]. In the current research landscape (Table 1), seven major categories of cathode materials have been explored in the design of nonaqueous AIBs, namely, carbon-based materials, transition-metal sulfides/oxides, organic compounds, heterojunction materials, MOFs/COFs and their deriva-

Table 1 Classification of cathodes used in nonaqueous AIBs and their electrochemical performance.

Classification	Cathode	Electrolyte	Battery type	Loading (mg cm^{-2})	Voltage range (V)	Current density (mA g^{-1})	Initial capacity (mAh g^{-1})	Cycle number	Final capacity (mAh g^{-1})	Ref.
Carbon-based cathodes	Graphite nanosheets	$AlCl_3$:[EMIm]Cl = 1.3:1	Swagelok	N/A	0–2.5	10,000	133	6700	121	[42]
	Graphite	$AlCl_3$:[EMIm]Cl = 1.3:1	CR2025	N/A	0.01–2.4	1000	72.5	10,000	72.5	[43]
	2D layered graphene/TiO_2 nanosheets composite	$AlCl_3$:[EMIm]Cl = 1.3:1	CR2032	2	0.1–0.9	1000	61	100	40	[44]
Transition-metal sulfide and oxide cathodes	S-NiCo@reduced graphene oxide	$AlCl_3$:[EMIm]Cl = 1.3:1	Swagelok	N/A	0.1–2.3	1000	248.2	100	83	[45]
	1D nanorod-like Sb_2S_3	$AlCl_3$:[EMIm]Cl = 1.3:1	Swagelok	N/A	0.2–1.8	1000	170	220	363	[46]
	VS_4 nanowire clusters	$AlCl_3$:[EMIm]Cl = 1.3:1	CR2016	1.32	0.1–1.8	400	50	120	129.24	[47]
	Niobium carbide (Nb_2CT_x)–MoS_2	$AlCl_3$:[BMIm]Cl = 1.5:1	Pouch cell	N/A	0.5–2.8	100	500	500	350	[48]
	FeS_2@carbon nanotube networks	NaCl:KCl:$AlCl_3$ = 26:13:61	Swagelok	1	0.1–1.8	500	191.2	800	171.3	[49]
Organic-based cathodes	Oligomeric naphthalene	$AlCl_3$:[EMIm]Cl = 1.3:1	Swagelok	1.5	0.1–2.3	1000	199	4500	175	[39]
	$FeVO_4$@polyaniline nanobelt composite	$AlCl_3$:[EMIm]Cl = 1.3:1	N/A	1.24	0–2	300	226	300	300	[50]
	Polyphenylene	$AlCl_3$:[EMIm]Cl = 1.3:1	N/A	1	0.01–2	10,000	65	30,000	61	[51]
Heterojunction cathodes	Cu_2Se@MnSe heterojunction hollow spherical shell	$AlCl_3$:[EMIm]Cl = 1.3:1	Swagelok	0.5	0.1–2.4	1000	418.01	3000	114.01	[38]
	$MnSe_2$–MnSe heterojunction hollow spheres	$AlCl_3$:[EMIm]Cl = 1.3:1	Swagelok	N/A	0.1–2.4	1000	436.01	3000	103.76	[52]
	Cyclodextrin polymer@$FeSe_2$/$CoSe_2$	$AlCl_3$:[EMIm]Cl = 1.3:1	Swagelok	0.3	0.1–2.4	1000	193	2200	167	[53]
MOF, COF, and their derivative cathodes	3D-ordered macroporous cobalt diselenide@carbon	$AlCl_3$:[EMIm]Cl = 1.3:1	Swagelok	1	0.05–2.2	2000	168	1000	125	[54]
	Hierarchical porous carbon octahedrons	$AlCl_3$:[EMIm]Cl = 1.3:1	CR2032	3.25	0.8–2.25	1000	40	1000	35.6	[55]
	2D Cu-based MOFs	$AlCl_3$:[EMIm]Cl = 1.3:1	Swagelok	1	0.1–2.2	200	160	1000	155	[56]
	2,6-diaminoanthraquinone–1,3,5-triformylphloroglucinol COF	$AlCl_3$:[EMIm]Cl = 1.3:1	Swagelok	0.5	0.3–2.2	10000	160	32000	170	[57]
	Triphenylamine–COFs	$AlCl_3$:[EMIm]Cl = 1.3:1	N/A	N/A	0.1–2.4	1000	161.2	3000	138	[40]

Note: [BMIm]Cl, 1-butyl-3-methylimidazolium chloride. 1D/2D/3D, 1/2/3 dimensional. All the anodes are Al.

tives, MXenes, and chalcogen elements (S/Te). In the following sections, we systematically elucidate the underlying operational mechanisms, present representative examples, evaluate the electrochemical performance, and discuss established chemistry–structure–property relationships for each category.

2.1 Carbon-based cathodes

Carbon-based materials are promising cathode materials for nonaqueous AIBs owing to their high electrical conductivity, tunable pore structure, and excellent cycling stability. These materials include graphite, graphene, carbon nanosheets, and carbon nanotubes. Graphite materials have the advantages of a high power density, good cycling performance, low cost, and strong ion-intercalation ability, ranking them among the most promising cathode materials for nonaqueous AIBs. Their energy-storage mechanism typically involves the intercalation and deintercalation of aluminum chloride anions (such as $AlCl_4^-$) between the layers of the carbon materials.

Wang et al.[42] described the preparation of graphite nanosheets (GNS-20) via supercritical carbon dioxide exfoliation of graphite. The graphite nanosheets were used as cathode materials for high-performance nonaqueous AIBs (Fig. 2a). Exfoliation using supercritical carbon dioxide effectively separates the graphite layers while minimizing damage to the material, and the rapid pressure release increases the interlayer spacing of graphite. The porosity of the graphite nanosheets, which crucially affects the performance of the AIBs, can be tuned by adjusting the exfoliation pressure. As illustrated in Fig. 2b, at an exfoliation pressure of 20 MPa, GNS-20 has a porosity of 86.7%, which is significantly higher than that of the congeners prepared at 15 MPa (GNS-15, 71.5%) and 10 MPa (GNS-10, 69.7%). Higher porosity facilitates intercalation and diffusion of the tetrachloroaluminate ions, leading to improved electrochemical performance. The capacitance contribution rate of GNS-20 reached 89.7% at a scan rate of 0.5 mV s^{-1}, and the capacitance contribution rate gradually increased with increasing scan ratio (Figs. 2c and 2d). This indicates that the higher electrical conductivity and more complete crystal structure of GNS-20 enhance capacitive energy storage, accelerate diffusion of the tetrachloroaluminate anion, and contribute to the excellent rate performance of the battery. Moreover, at an ultrahigh current density of 10 A g^{-1}, the battery maintained a specific discharge capacity of 131 mAh g^{-1} after 6700 cycles, demonstrating excellent cycling stability. The proposed method is effective and environmentally friendly and has great potential in various applications.

Zhang et al.[43] presented a green, low-cost water-washing method for regenerating graphite from spent LIBs and demonstrated the successful application of the regenerated graphite as a cathode material for nonaqueous AIBs (Fig. 2e). The key concept was the preparation of graphite with a slightly expanded interlayer spacing, which accommodates large $AlCl_4^-$ anions more easily, reduces the diffusion energy barrier, and promotes faster ion kinetics. Coin cells employing graphite as the matched electrode demonstrated excellent rate and cycling performance (Figs. 2f and 2g). Notably, the cells could withstand over 10,000 cycles at a current density of 1000 mA g^{-1}, delivering an average capacity of 72.5 mAh g^{-1} with no significant degradation. Although the graphite or graphene-based cathode materials used in nonaqueous AIBs have high discharge voltages as well as high cycling and rate performance, these batteries have the following problems: (1) low capacity; (2) side-reactions at high cut-off voltages (>2.4 V); (3) self-discharge (arising primarily from the severe lattice strain caused by $AlCl_4^-$ intercalation, which promotes spontaneous deintercalation to release stress when standing); and (4) poor coulombic efficiency at low current densities. These problems hinder the practical application of carbon-based materials in nonaqueous AIBs.

2.2 Transition-metal sulfide and oxide cathodes

Transition-metal oxides and sulfides, as novel electrode materials, demonstrate unique energy-storage advantages and immense application potential. These materials are abundant in the Earth's crust, have low raw material costs, and can be produced on a large scale using simple preparation methods such as hydrothermal synthesis, co-precipitation, and solid-state sintering. Their synthesis pathways are flexible and exhibit strong process compatibility. These materials possess a diversity of crystal structures, ranging from layered (e.g., MoS_2, V_2O_5) and spinel (e.g., Mn_3O_4) to tunnel structures (e.g., TiO_2), providing tunable intercalation channels and active sites for ion storage. Notably, compared to traditional carbon-based cathode materials, transition-metal compounds demonstrate outstanding electrochemical performance. Their energy-storage mechanism comprises anion intercalation/deintercalation reactions and often involves multielectron-transfer redox processes, enabling the storage of more charge per unit mass. Consequently, these materials often exhibit high specific capacities during the initial discharge, exceeding 200 mAh g^{-1}, and are considered highly promising cathode candidates for nonaqueous AIBs.

2.2.1 *Transition-metal-sulfide cathodes*

Compared with transition-metal oxides, the ionic radii of sulfur and selenium in transition-metal sulfides and selenides are larger, and their electrostatic interaction with Al^{3+} ions is weaker, which is more conducive to the intercalation/deintercalation of Al^{3+}. Moreover, transition-metal sulfides have advantages such as high theoretical capacity and high energy density when used as electrodes in nonaqueous AIBs. Therefore, transition-metal sulfides have greater potential as cathode materials for nonaqueous AIBs.

Xing et al.[45] grew NiCo-layer double hydroxides nanosheets directly on graphene oxide (GO) via a hydrothermal method to form a hierarchical structure, which was then controllably sulfided to obtain the binary metal sulfide (S-NiCo@reduced graphene oxide [rGO]) for use in the cathode (Fig. 3a). As depicted in Fig. 3b, the S-NiCo@rGO components maintained the original nanosheet morphology, but their size was significantly reduced owing to the presence of GO during synthesis, which is highly beneficial for Al^{3+} diffusion, electron transfer, and electrolyte penetration. Analysis of the cyclic voltammetry (CV) curves and the relationship between the peak current and scan rate demonstrated that the reaction of the S-NiCo@rGO electrode was highly reversible and diffusion-

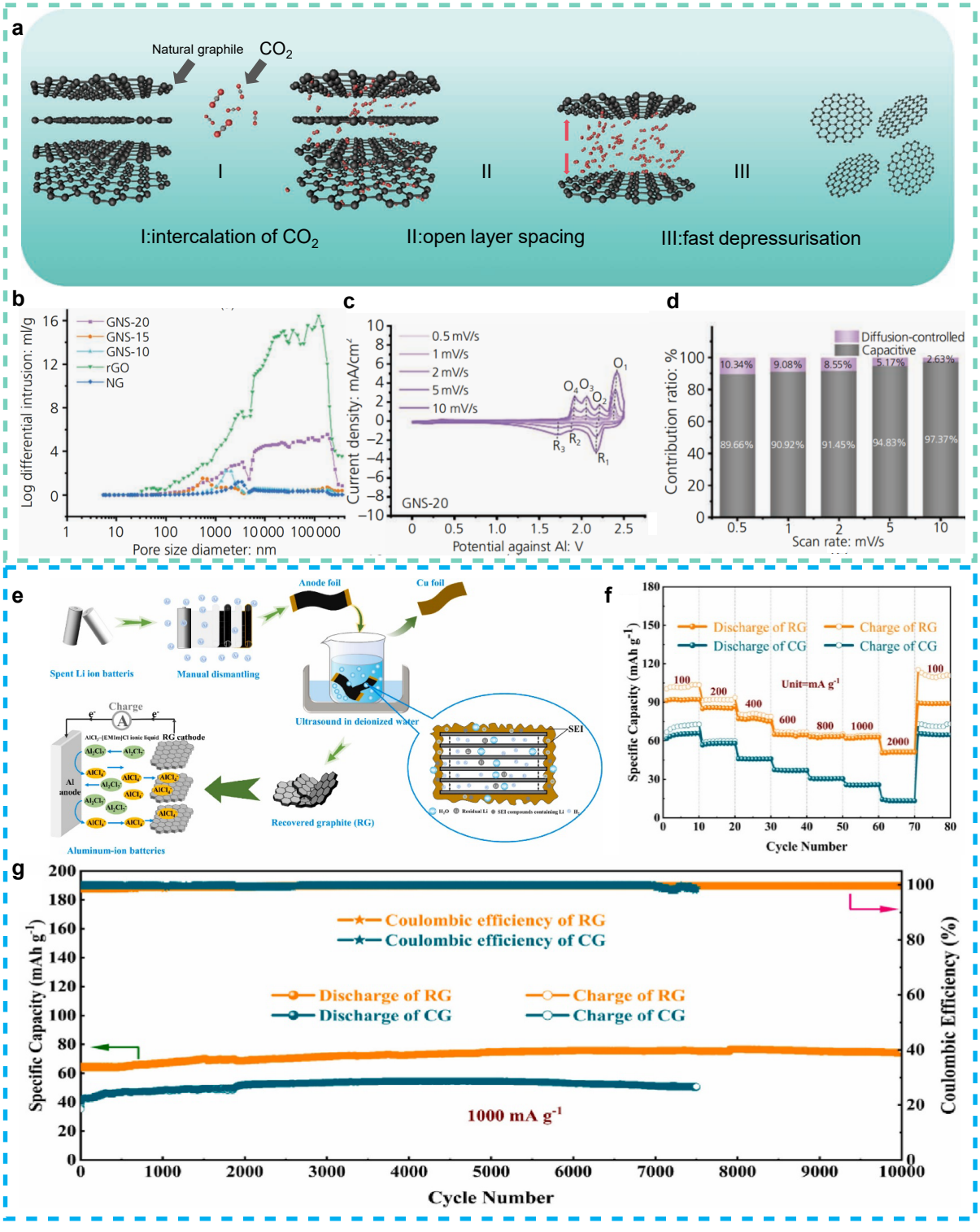

Figure 2 (a) Schematic of ultrasound-assisted supercritical carbon dioxide stripping of graphite nanosheets. (b) Mercury intrusion porosimetry curves of GNS-20, GNS-15, GNS-10, rGO, and NG samples. GNS-10, GNS-15, and GNS-20 samples were obtained by exfoliating graphite nanosheets with supercritical CO_2 at 10, 15, and 20 MPa, respectively. (c) Cyclic voltammetry (CV) curves of three samples of GNS-20 and (d) energy-storage mechanisms of GNS-20. Reproduced with permission from Ref. [42] ©2024, Emerald Publishing. (e) Schematic of graphite recovery from spent lithium battery. (f) Rate performance of commercial CG and recovered RG. (g) Performance curves of CG and RG for 7500 and 10,000 cycles at a current density of 1000 mA g^{-1}. Reproduced with permission from Ref. [43] ©2024, Published by Elsevier Ltd.

controlled (Fig. 3c). As shown in Fig. 3d, the initial discharge capacity of the obtained S-NiCo@rGO reached 248 mAh g^{-1}at a current density of 1 A g^{-1} while maintaining a reversible discharge capacity of 83 mAh g^{-1} after 100 cycles, with a coulombic efficiency close to 100%.

Although cathodes comprising transition-metal sulfides

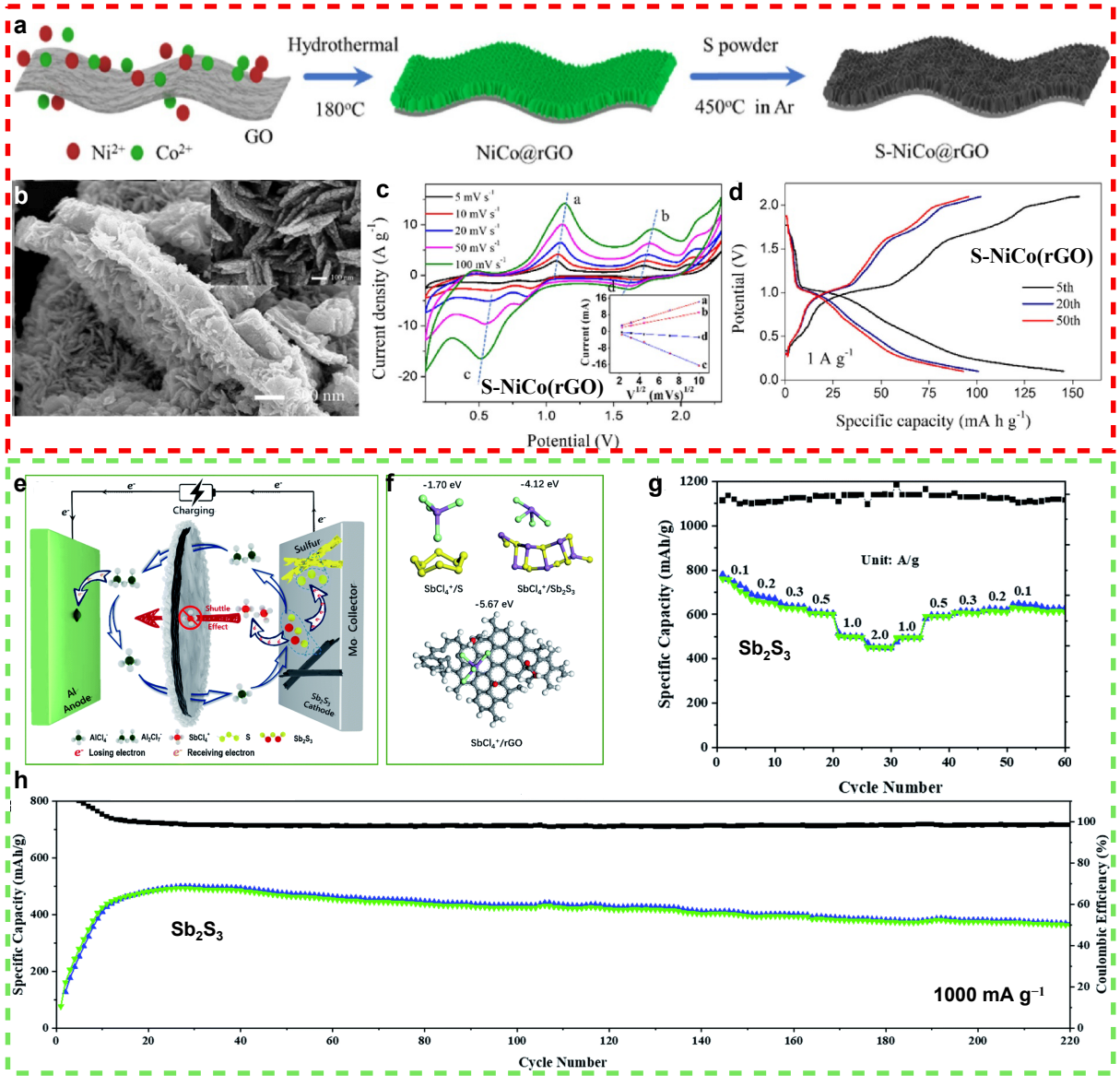

Figure 3 (a) Schematic of preparation of S-NiCo@reduced rGO. (b) Scanning electron microscopy images of S-NiCo@rGO. (c) CV curves at scan rates of 5–100 mV s^{-1}, inset shows relationship between current and scan rate. (d) Charge and discharge curves of S-NiCo@rGO at the 5th, 20th, and 50th cycles at a current density of 1000 mA g^{-1}. Reproduced with permission from Ref. [45] ©2020, Elsevier Ltd. (e) Schematic of energy-storage mechanism of Sb_2S_3 cathode during charging. (f) Theoretical calculations of the adsorption energies and structures of $SbCl_4^+$ adsorbed on S, Sb_2S_3, and rGO. Electrochemical performance of Sb_2S_3: rate performance at different current densities (g) and cycle performance at 1000 mA g^{-1} (h) . Reproduced with permission from Ref. [46] ©2022, The Royal Society of Chemistry.

afford a higher initial battery capacity than carbon-based cathodes, the dissolution and diffusion of polysulfides during battery cycling lead to severe loss of the active materials from the cathode. This leads to rapid capacity fading after the initial few cycles and poor cycling performance. To address this issue, Li et al.[46] utilized a solvothermal method to synthesize well-crystallized, one-dimensional, nanorod-shaped Sb_2S_3 for use as cathode material and introduced a graphene aerogel (GA) intermediate layer between the cathode and separator (Fig. 3e). Owing to the mixed reversible redox reaction of Sb-related cations (Sb(+3) ⇔ Sb(+5)) and S-related anions (S(−2) ⇔ S(0)), the Sb_2S_3 cathode achieved a mixed 10-electron transfer reaction, with a theoretical capacity as high as 786 mAh g^{-1}, approaching its theoretical limit (789 mAh g^{-1}). Additionally, the GA intermediate layer provided a dual physical–chemical barrier wherein its porous structure blocks the migration of $SbCl_4^+$ to the anode and density functional theory (DFT) calculations indicate that its oxygen-containing functional groups anchor $SbCl^{4+}$ via chemical adsorption (adsorption energy −5.67 eV), effectively stabilizing the soluble products and mitigating the "shuttle effect" (Fig. 3f). This novel Sb_2S_3 cathode exhibited excellent rate and cycling performance, maintaining a capacity of 363 mAh g^{-1} after 220 cycles at 1000 mA g^{-1}, with a coulombic efficiency close to 100%. This design offers a new approach for breaking the capacity limit of cathode materials (Figs. 3g and 3h).

Alongside cathodes comprising sulfide materials with nanosheet and nanorod structures, other low-dimensional nanostructures, such as nanoclusters and nanotubes, have also been the focus of many studies. Specifically, these zero- and one-dimensional architectures provide a high surface-to-volume ratio and abundant active sites, which significantly shorten the diffusion pathways for Al-complex ions. Moreover, the hollow or porous interior of these nanostructures can effectively accommodate the large volume expansion typically associated with the intercalation of bulky $AlCl_4^-$ or $Al_xCl_y^-$ species, mitigating mechanical strain and preventing electrode pulverization during prolonged cycling. The unique structural features of these materials endow them with the potential for excellent electrochemical performance. The following section systematically elaborates research progress related to these two types of sulfide cathode materials.

Using an amine-ion-assisted method, Xing et al.[47] synthesized a vanadium sulfide (VS_4) nanowire cluster cathode rich in ion channels. Transmission electron microscopy (TEM) images show that VS_4 has a porous surface structure with a uniform distribution of V and S (Figs. 4a and 4b). The rough surface promotes close contact between the electrode and the electrolyte, thereby facilitating excellent rate performance. The system maintained 103.32 mAh g^{-1} even at a high-current density of 800 mA g^{-1} (Fig. 4c). Although this ingenious nanostructural design significantly enhanced the ion diffusion and the structural stability, it remains limited by the intrinsic low conductivity of the active material. To address this deficiency, Ming et al.[49] developed a binder-free pyrite (FeS_2)@carbon nanotube (CNT) self-supporting structure as a cathode material through an *in situ* growth strategy. This structure comprises a unique three-dimensional conductive network of functionalized CNTs (F-CNT) and eliminates binder-induced side-reactions, thereby affording significantly improved conductivity. As shown in Fig. 4d, FeS_2 is uniformly and densely distributed on the surface of F-CNT, with particle sizes of 1–2 μm. The energy-dispersive spectroscopy (EDS) data indicate a

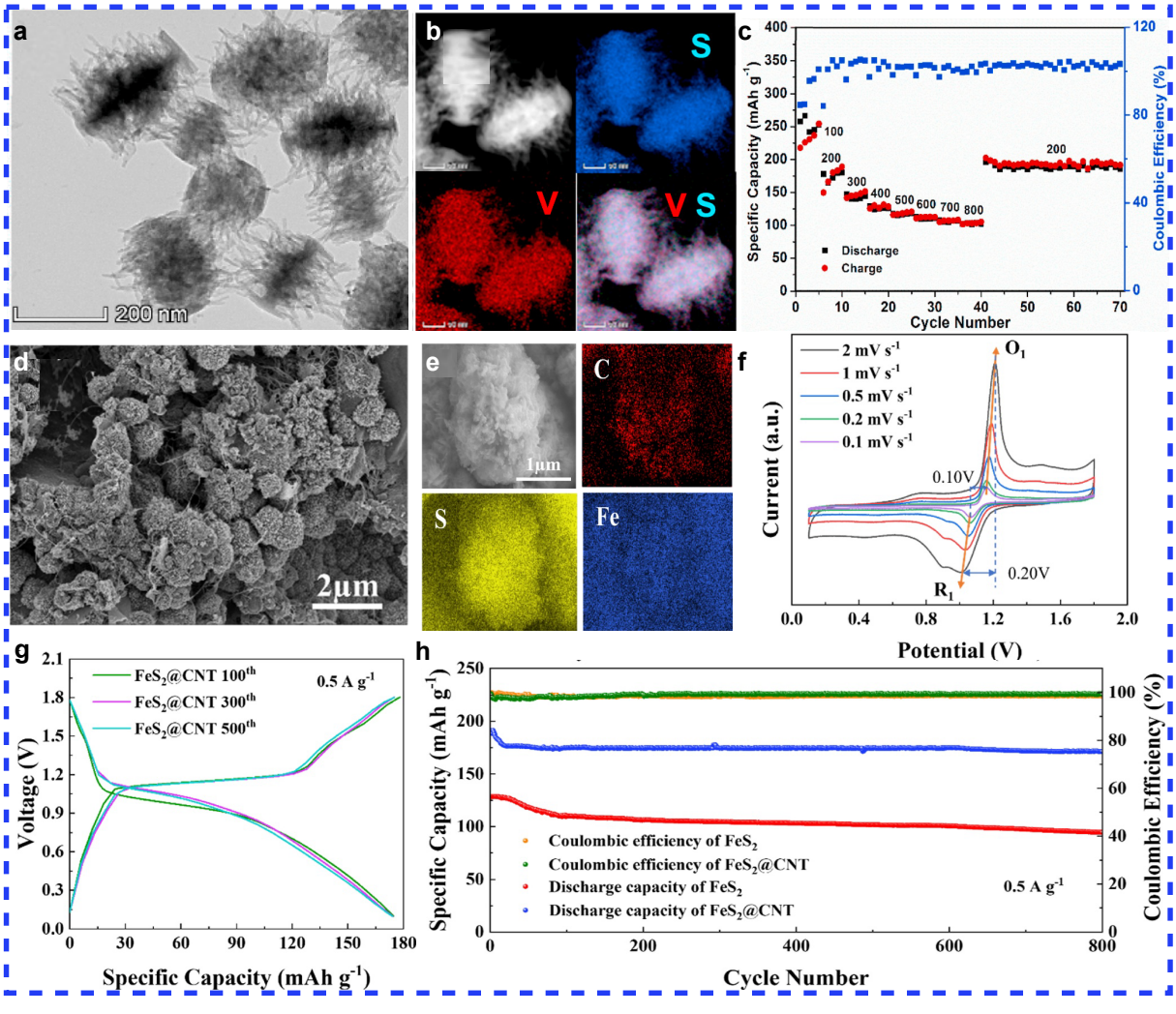

Figure 4 TEM (a) and high-angle annular dark-field scanning transmission electron microscopy (HAADF-STEM) (b) images and corresponding elemental mapping images of VS_4 nanowire clusters. (c) Rate performance of VS_4 nanowire clusters at various current densities. Reproduced with permission from Ref. [47] ©2020, Elsevier Ltd. Scanning electronic microscopy (SEM) (d) and energy-dispersive spectroscopy (EDS) (e) images of FeS_2@carbon nanotube networks. (f) CV curves of FeS_2@CNT at different scan rates during cyclic stabilization. (g) Charge/discharge curves of FeS_2@CNT at the 100th, 300th, and 500th cycles at 0.5 A g^{-1}. (h) Cycling performance of FeS_2 and FeS_2@CNT at 0.5 A g^{-1}. Reproduced with permission from Ref. [49] ©2025, The Electrochemical Society.

uniform distribution of iron, sulfur, and carbon in FeS2@CNT (Fig. 4e). The CV curve in Fig. 4f shows that the CNT network significantly enhanced the reactivity of the FeS_2 electrode, reduced polarization, and maintained rapid, stable, and reversible reactions. At a high-current density of 0.5 A g^{-1}, the FeS_2@CNT cathode exhibited an outstanding initial discharge capacity of 191.2 mAh g^{-1}. After 800 cycles, FeS_2@CNT maintained a high discharge capacity of 171.3 mAh g^{-1} (Figs. 4g and 4h). This three-dimensional, self-supporting, binderless composite electrode with an independent current collector represents a paradigm shift in the design of nonaqueous AIBs electrodes. In the future, the breakthrough for achieving high-performance electrodes may no longer be limited to the discovery of higher-capacity active materials but may lie in the inherent properties of the electrode, for addressing various challenges.

The abovementioned studies are based on button cells or Swagelok cells. By optimizing the structure and regulating the composition of the cathode materials, they addressed the key challenges faced by nonaqueous AIBs, including sluggish kinetics, volume expansion, and difficulty in ion intercalation, achieving significant research progress. However, to advance the practical application of these material systems, tests at the button-cell level are often insufficient for comprehensive evaluation of their overall performance in actual device environments. Against this backdrop, Mahar et al.[48] made a crucial leap from material innovation to device validation. This team constructed the first example of a Nb_2CT_x-MoS_2 composite cathode using a fluorine-free, green method. This design combines the advantageous high conductivity and wide interlayer spacing of Nb_2CT_x with the pseudocapacitive properties of MoS_2, achieving a synergistic improvement in the ion transport and structural stability. Using an $AlCl_3$/[BMIm]Cl (1.5) ionic-liquid electrolyte, they assembled a 2 inch × 2 inch aluminum-ion pouch cell, solving the capacity decay problems caused by distortion of the cathode lattice and corrosion of the anode in traditional nonaqueous AIBs. This composite cathode delivered a high specific capacity of ~350 mAh g^{-1} at 100 mA g^{-1} and demonstrated exceptional cycling stability, retaining nearly 98% coulombic efficiency over 500 cycles. That study introduced key material design concepts for furthering the development of high-performance, long life, and low-cost aluminum-ion pouch cells.

2.2.2 *Transition-metal-oxide cathodes*

Compared with metal sulfides or selenides, transition-metal oxides are ideal cathode materials for nonaqueous AIBs because of their high stability in ionic liquids, simple preparation, and nontoxicity. However, owing to the strongly polar metal bonds in transition-metal oxides, the cathode materials undergo volume expansion and significant lattice distortion during repeated charge and discharge, eventually leading to structural collapse of the electrode and decreased electrochemical cycling performance. Therefore, the types of transition-metal oxides available for use as electrode materials in nonaqueous AIBs are very limited.

To improve the application of transition-metal oxides as cathode materials in nonaqueous AIBs, Xue et al. [44] designed a two-dimensional superlattice heterointerface composite structure comprising closely stacked layered graphene and titanium dioxide nanosheets. This structure possesses numerous lattice defects and phase interfaces, which can provide insertion channels and storage space for $Al_xCl_y^-$ polyanions. Interestingly, the $Al_xCl_y^-$ polyanions are stored at the two-dimensional heterointerface between the graphene and TiO_2 layers rather than within the bulk lattice. This design provides an excellent carrier, and the full cell exhibits superior performance, including a specific discharge capacity of up to 313.2 mAh g^{-1} at a current density of 0.1 A g^{-1}, with improved cycling performance.

Although transition-metal oxides and sulfides have shown great potential in nonaqueous AIBs, most are prone to dissolution in corrosive electrolytes, leading to poor battery cycling performance. To mitigate this, the cathode materials must maintain structural stability in ionic liquids or quasi-solid electrolytes. Tailoring the composition of the cathodes is an effective strategy for ensuring the structural stability of transition-metal oxide and sulfide cathodes and improving the cycling performance of nonaqueous AIBs.

2.3 Cathodes comprising organic materials

Although cathodes prepared from transition metals exhibit good electrochemical performance, issues such as nonrenewable resources, difficult battery recycling, high cost, and environmental unfriendliness persist. In contrast with inorganic cathode materials, the main components of organic electrode materials are C, H, O, and N. Organic cathodes have the advantages of abundant sources, simple synthesis and preparation, green and renewable nature, low cost, and structural diversity. Therefore, they have received extensive attention in recent years.

Based on changes in the charge state of the redox-active groups during charging and discharging, organic cathode materials can be roughly classified as n-type, p-type, or bipolar. During discharge, n-type organic compounds (such as carbonyl compounds, imine compounds, and organic sulfides) generally undergo an initial reduction to form anions. Subsequently, these anions interact with cations to maintain the charge neutrality of the electrolyte. Unlike the n-type materials, p-type organic electrode materials first undergo an oxidation process, losing electrons to form cations. The formed cations interact with anions to maintain the charge neutrality of the electrolyte. Bipolar organic electroactive materials possess the characteristics of both n-type and p-type materials. Conductive polymers are typical bipolar organic electrode materials. They can be reduced from the semioxidized state to the reduced state during discharging, and oxidized from the semioxidized state to the oxidized state during charging. However, their molecular design is relatively complex and research on their use in nonaqueous AIBs is still in the exploration stage.

Generally, the electrochemical performance of aluminum/organic batteries depends on their energy-storage mechanism. Compared with p-type and bipolar organic cathodes, n-type organic cathodes have a higher specific capacity and lower working voltage. However, n-type organic compounds undergo repeated bond breaking

and reforming during charging and discharging, leading to degradation of the molecular structure and a continuous capacity decline. In contrast, p-type organic cathodes undergo almost no bond rearrangement during charging and discharging and generally exhibit better reaction kinetics and structural stability. Additionally, because of their anion redox chemistry, p-type electrodes typically offer higher working voltages than n-type electrodes. P-type materials are the most widely reported organic materials for nonaqueous AIBs cathodes. Some typical p-type cathode materials are introduced below. Wang et al.[50] developed a novel one-dimensional $FeVO_4$@polyaniline (PANI) nanoribbon composite material, where dense PANI nanospikes were grown *in situ* on $FeVO_4$ nanoribbons as a cathode material. Figure 5a shows the uniform and dense PANI nanoneedle array constructed on the surface of the $FeVO_4$ nanoribbons, forming a unique three-dimensional hierarchical structure. This structure combines the advantages of the rapid axial transport of the one-dimensional nanoribbons with the large specific surface area and numerous active sites of the surface nanoneedle array, demonstrating excellent electrochemi-

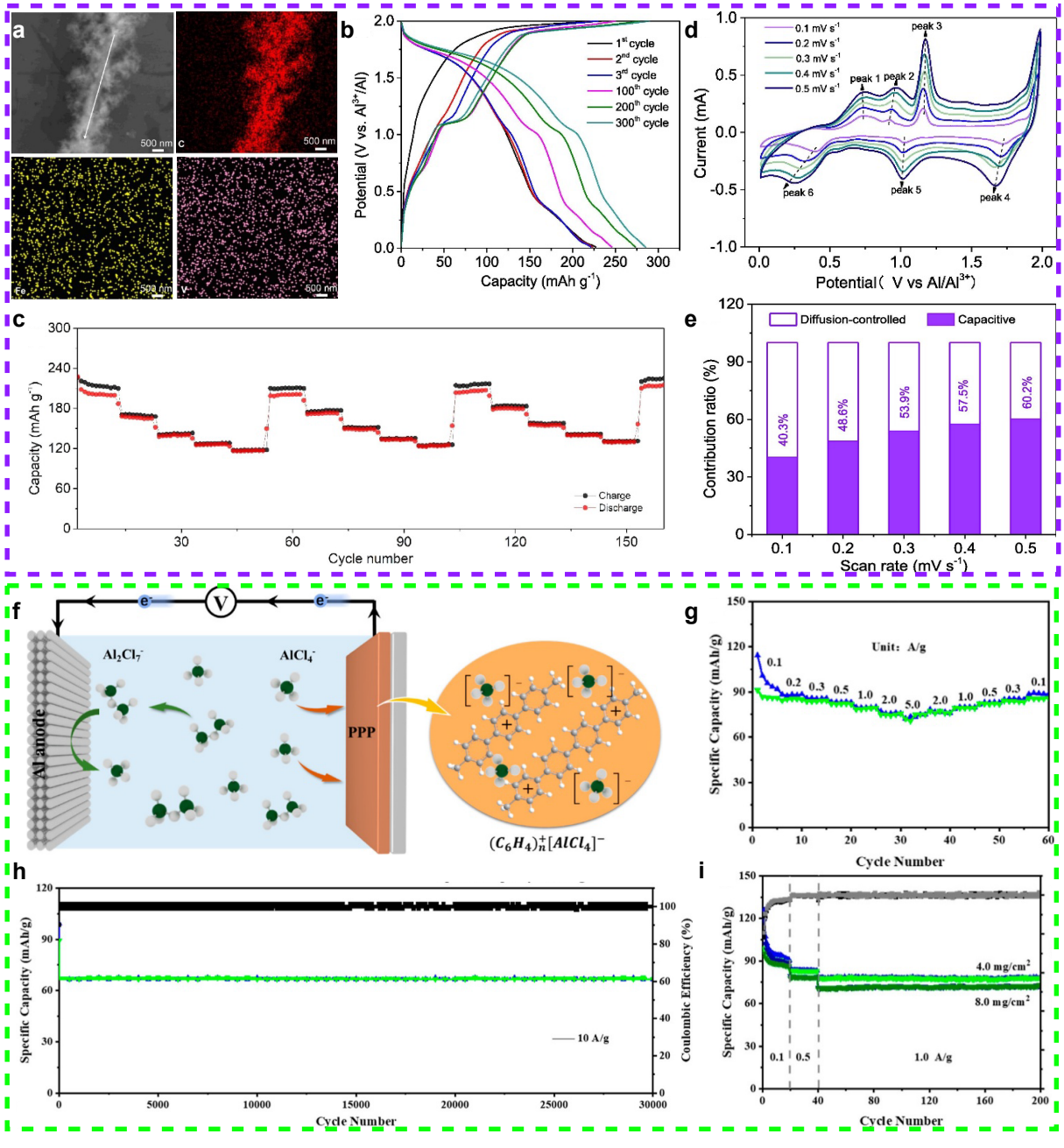

Figure 5 (a) SEM and elemental mapping images of C, Fe, and V in $FeVO_4$@PANI nanobelt composite. Charge–discharge profiles (b) and rate performance (c) of $FeVO_4$@PANI. (d) CV curves of $FeVO_4$@PANI at 0.1 to 0.5 mV s^{-1}. (e) Contribution ratio of capacitance control and diffusion control. Reproduced with permission from Ref. [50] ©2022, Elsevier B.V. (f) Schematic of energy-storage mechanism of polyphenylene (PPP) cathode during charging in nonaqueous AIBs. (g) Rate performance of PPP at different current densities. (h) Long-term performance of PPP cathode at 10 A g^{-1} over 30,000 cycles. (i) Discharge capacity of PPP electrodes with different loadings. Reproduced with permission from Ref. [51] ©2022, American Chemical Society.

cal performance as a cathode material for nonaqueous AIBs. During charging, the conjugated structure of PANI undergoes oxidation and electron loss, forming positively charged active sites (such as $-NH_2^+-$), which are charge-balanced by the insertion of $AlCl_4^-$ anions from the electrolyte. After 300 cycles at 0.3 A g^{-1}, the specific capacity of the $FeVO_4$@PANI cathode remained at 300 mAh g^{-1}, compared to 199.8 mAh g^{-1} for pure $FeVO_4$ (Fig. 5b). Additionally, the rate performance of the $FeVO_4$@PANI composite material remained stable after three cycles, attributed to the suitable environment provided by the PANI nanoneedle array on the surface, shortening the distance for ion and electron transfer and improving the conductivity (Fig. 5c). As shown in Figs. 5d and 5e, the CV curves maintained a good shape at scan rates from 0.1 to 0.5 mV s^{-1}, confirming the high reversibility of the reaction and structural stability of the electrode. The relationship between the peak current and scan rate is governed by the power law $i = av^b$, where i is the peak current, v is the reaction rate, and b is the kinetic parameter for the surface reaction. The calculated b value for the oxidation and reduction peaks was generally close to or higher than 0.5, indicating that the charge-storage process is mainly dominated by pseudocapacitive behavior rather than being limited by bulk diffusion, and the proportion of the capacitive contribution increases with increasing scanning speed.

However, materials such as PANI, having quinone or imine structures, suffer from severe dissolution in ionic electrolytes, especially during discharge, leading to loss of the active mass, which affects the cycling performance and coulombic efficiency of the cathode. To enhance the stability of the cathode, Li et al.[51] synthesized a conjugated polymer, polyphenylene (PPP), via the polymerization of benzene. PPP features a large interlayer spacing (4.53 Å), abundant mesopores, high chemical stability, and insolubility in Lewis acidic ionic-liquid electrolytes. In electrochemical redox processes, PPP undergoes oxidation by losing electrons to form radical cations $[C_6H_4]_{3n}^+$, which are stabilized through the intercalation of $[AlCl_4]^-$ to maintain charge neutrality, thereby enabling efficient electrochemical energy storage (Fig. 5f). Owing to the intercalation of $[AlCl_4]^-$, the PPP cathode provides a relatively high working voltage of approximately 1.4 V. The PPP cathode demonstrates excellent rate performance and, at an ultrahigh current density of 10 A g^{-1}, shows almost no capacity decay after 30,000 cycles (Figs. 5g and 5h). Furthermore, as shown in Fig. 5i, the Al-PPP battery maintains stable cycling performance and high reversible capacity at a high active-material loading (4 and 8 mg cm^{-2}).

However, the energy density of the aforementioned organic cathode materials is relatively low, which limits their practical application. To increase the energy density, the operating voltage of organic cathode materials must be increased by shifting the focus from "regulating the molecules themselves" to "regulating how the molecules assemble". Wang et al.[39] used π-conjugated organic compounds as a model of oligomeric naphthalene (ONA) with intermolecular π–π stacking structures for a high-voltage aluminum-ion energy-storage system (Fig. 6a). *In situ* Raman spectroscopy (Figs. 6b–6d) revealed the unique two-step "adsorption-intercalation" energy-storage mechanism and high reversibility of the ONA electrode. Analysis of the kinetics of the electrochemical reaction (Figs. 6e and 6f) indicated that the energy-storage process in the ONA electrode was co-dominantly dictated by surface control (pseudocapacitance) and diffusion control, with a b value (0.82–0.89) between the two. As the scan rate increased, the pseudocapacitive contribution increased from 59.7% to 76.8%, demonstrating that the material effectively maintained efficient charge storage at high rates. Mechanistic analysis revealed a two-step charge-storage process involving initial adsorption of $AlCl_4^-$ on the ONA molecules at low voltage, followed by the formation of $\pi\cdots[AlCl_4]\cdots\pi$ interactions with the π–π stacked structure at high voltage. This sequential mechanism afforded outstanding battery performance, characterized by a discharge plateau of ~1.9 V, high specific capacity of 450 mAh g^{-1} at 100 mA g^{-1}, and capacity retention of 170 mAh g^{-1} at 2000 mA g^{-1} (Fig. 6g). The ONA cathode exhibited outstanding cycling stability (achieving a capacity retention of 94.5% after 4500 cycles). As the number of cycles increased, the electrochemically active interface of the ONA cathode gradually expanded. The material self-adjusts and reorganizes into a nanoporous structure, providing more channels for ion transport and charge transfer (Figs. 6h and 6i). This study was the first to reveal that the intermolecular π–π stacking structure in π-conjugated organic materials can serve as a direct, high voltage, active energy-storage site, surpassing its traditional perception as playing a "supporting role" and opening up a new research direction where π–π stacking provides a novel energy-storage site.

2.4 Heterojunction cathodes

Selenide materials are recognized as promising cathode materials for nonaqueous AIBs owing to their high energy density, excellent electrochemical activity, and simple preparation processes. However, in practical applications, selenides undergo significant volume expansion during electrochemical reactions. Selenides are also highly soluble in $AlCl_3$/[EMIm]Cl ionic electrolytes, leading to irreversible loss of the active materials and the subsequent shuttle effect, a major factor limiting battery capacity. To address this challenge, Lei et al.[58] modified the separator using CMK-3 carbon material, which effectively suppressed the shuttle effect but failed to curtail selenide dissolution. In contrast, Li et al. introduced heterojunction structures into selenide cathodes to fabricate $MnSe_2$–MnSe heterojunction spherical shells via hydrothermal synthesis, followed by selenization[52]. These $MnSe_2$–MnSe heterojunction spherical shells not only inhibit the shuttle effect caused by selenide dissolution but also restrict diffusion of the active materials, thereby enhancing the cycling stability of the battery (Fig. 7a). Experiments demonstrated that the ion-diffusion coefficient of the $MnSe_2$–MnSe heterojunction hollow spheres is higher than that of pure $MnSe_2$ and MnSe, indicating more efficient ion transport and charge transfer in the former during electrochemical reactions (Fig. 7b). Building on this research, Li et al. further developed Cu_2Se@MnSe heterojunction hollow spherical shell cathodes and cyclodextrin polymer (β_{CD})@$FeSe_2$/$CoSe_2$ heterostructured cathodes

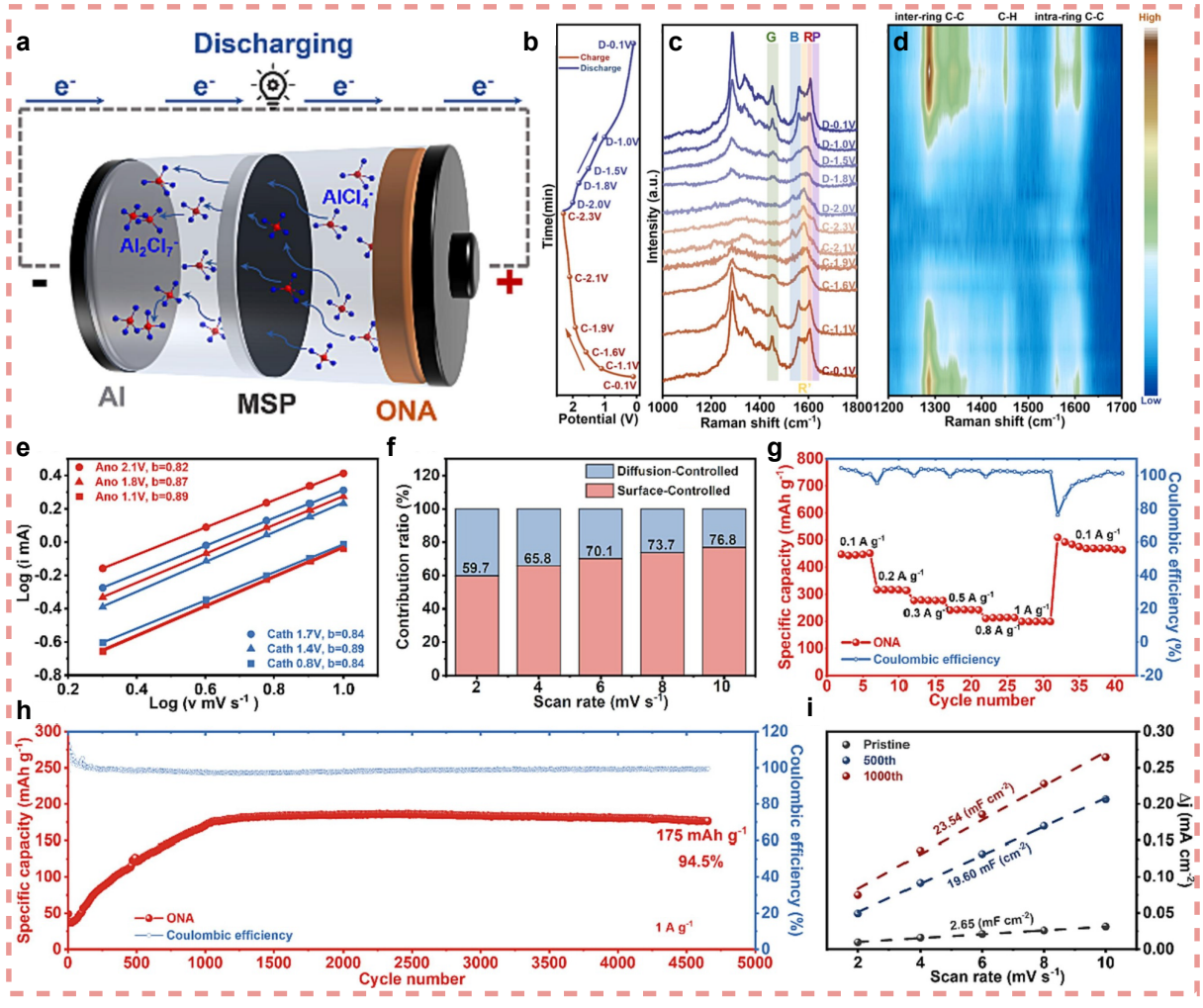

Figure 6 (a) Diagram of working mechanism of Al-ONA battery. MSP, modified separators (b) Charge–discharge curve of ONA electrode in an *in situ* cell. (c) *In situ* Raman spectrum and (d) contour and response surface analysis of ONA electrode corresponding to the discharge–charge process. (e) Determination of *b* values from the peak current versus scan rate. (f) Normalized proportion of contribution of surface-controlled and diffusion-controlled charge storage at different scan rates for the ONA electrode. (g) Specific capacity and coulombic efficiency of ONA cathode at current densities from 0.1 to 1 A g^{-1} (data were collected after stabilization for 15 cycles at 100 mA g^{-1}). (h) Cycling performance and coulombic efficiency of ONA cathode at a current density of 1 A g^{-1} (voltage window: 0.1–2.3 V). (i) Electrochemically active interface. Reproduced with permission from Ref. [39] ©2024, Elsevier B.V.

based on organometallic frameworks (Figs. 7c and 7e)[38,53]. The Cu_2Se@MnSe heterojunction hollow spherical shells effectively alleviated volume expansion of the selenides during charge–discharge cycling, affording cycling performance significantly superior to that of the pristine selenide cathodes. In comparison, the initial capacity of the β_{CD}@$FeSe_2$/$CoSe_2$ heterostructured cathode material is lower than that of the two aforementioned materials. Nevertheless, the β_{CD}@$FeSe_2$/$CoSe_2$ heterostructured cathode exhibits much higher-capacity retention in long-cycle tests compared to the aforementioned heterojunction materials. The galvanostatic intermittent titration technique (GITT) curves in Figs. 7d and 7f demonstrate that the Cu_2Se@MnSe heterojunction hollow spheres and β_{CD}@$FeSe_2$/$CoSe_2$ heterostructures exhibit a high ionic diffusion rate when employed as cathode materials. Li et al.[59] developed ZnSe/$SnSe_2$ heterojunction hollow microcubes, which simultaneously addressed the susceptibility of ZnSe to agglomeration and the severe volume effects in $SnSe_2$. The heterojunction structures efficiently mitigated the critical drawbacks of selenide cathodes, namely, high solubility and severe volume expansion, making the development of such structures a highly promising research direction in the field of AIBs materials.

2.5 Cathodes comprising MOFs, COFs, and their derivatives

MOFs are a class of porous crystalline materials that self-assemble from metal ions/clusters and organic ligands via coordination bonds. Featuring a high specific surface area, tunable pore size, diverse architectures, and functionality, the robust frameworks of MOFs can confine macromolecules. These distinctive properties render MOFs highly attractive in the field of electrochemical energy storage, particularly for battery applications[60–63]. As skeleton materials with high porosity, MOFs and their derivatives can serve as electrode materials, electrolytes, or separators in various battery systems. MOFs and their derivatives have been employed as cathode materials in nonaqueous

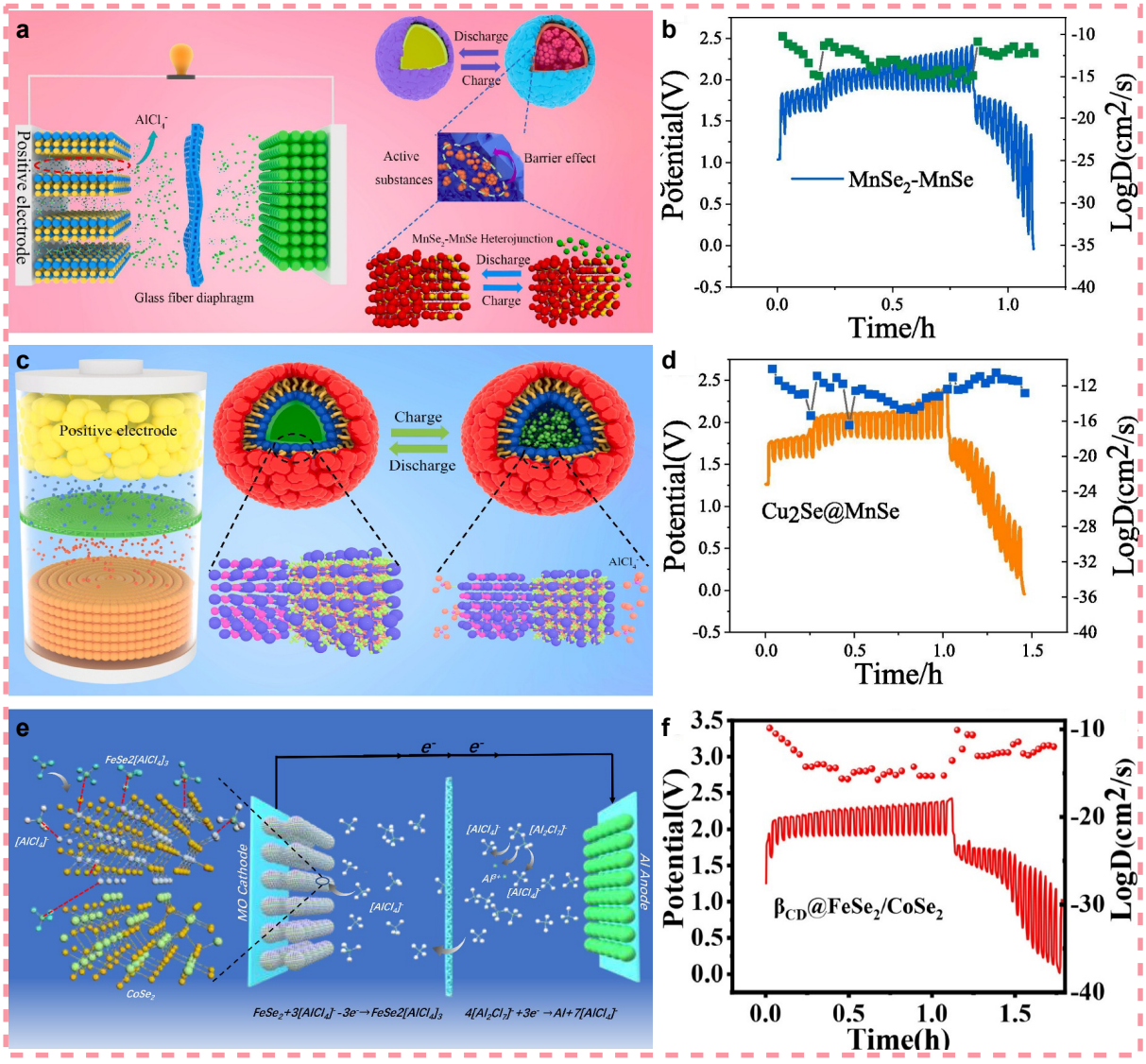

Figure 7 (a) Operational mechanism of $MnSe_2$–MnSe heterojunction. (b) Galvanostatic intermittent titration technique (GITT) curves of $MnSe_2$–MnSe. Reproduced with permission from Ref. [52] ©2023, Elsevier, Inc. (c) Operational mechanism of Cu_2Se@MnSe heterojunction hollow spherical shell. (d) GITT curve of $MnSe_2$–MnSe. Reproduced with permission from Ref. [38] ©2023, Elsevier B.V. (e) Schematic of β_{CD}@$FeSe_2$/$CoSe_2$ during charging. (f) GITT curve of β_{CD}@$FeSe_2$/$CoSe_2$. Reproduced with permission from Ref. [53] ©2024, Acta Materialia Inc.

AIBs for the storage of $AlCl_4^-$. However, the direct application of pristine MOFs as cathodes is severely hampered by inherent drawbacks, including low electrical conductivity, poor structural stability, and sluggish ion-transport kinetics. The prevailing strategy for addressing these issues is to utilize MOFs as precursors, which are subsequently converted to metal compounds (oxide, sulfide, and selenide)@carbon composites via carbonization, sulfidation, or selenization. This approach preserves the porous structure and active sites of the MOFs and remediates the performance deficiencies associated with their direct utilization. Hong et al.[54] mixed and heated single-crystal zeolitic imidazolate framework-67 (SOM ZIF-67) with selenium powder to obtain 3D-ordered macroporous cobalt diselenide@carbon (3DOM $CoSe_2$@C) (Fig. 8a), which was subsequently employed as a cathode material (Fig. 8b). The distribution of Co, Se, C, and C in the material is shown in Fig. 8c. N is uniformly distributed throughout the three-dimensionally ordered macroporous framework of 3DOM $CoSe_2$@C. The resultant 3DOM $CoSe_2$@C delivers an initial discharge capacity of 400 mAh g^{-1} at 1.0 A g^{-1}, retains a reversible capacity of 125 mAh g^{-1} after 1000 cycles at 2 A g^{-1}, and achieves a coulombic efficiency of nearly 96%. Endowed with a high specific surface area, rapid mass transfer channels, and a stable conductive framework, 3DOM $CoSe_2$@C breaks the bottleneck of limited $AlCl_4^-$ diffusion, thus realizing excellent rate capability and long-term cycling stability (Fig. 8d).

Wang et al.[55] fabricated hierarchical porous carbon octahedrons (HPCOs), a type of MOF derivative, via calcination (Fig. 9a). The HPCOs possess a hierarchical porous structure, and the embedded heteroatoms enhance the wettability and electrical conductivity of the material. Consequently, the HPCOs maintained a reversible specific capacity of 60.8 mAh g^{-1} after 200 cycles at 100 mA g^{-1},

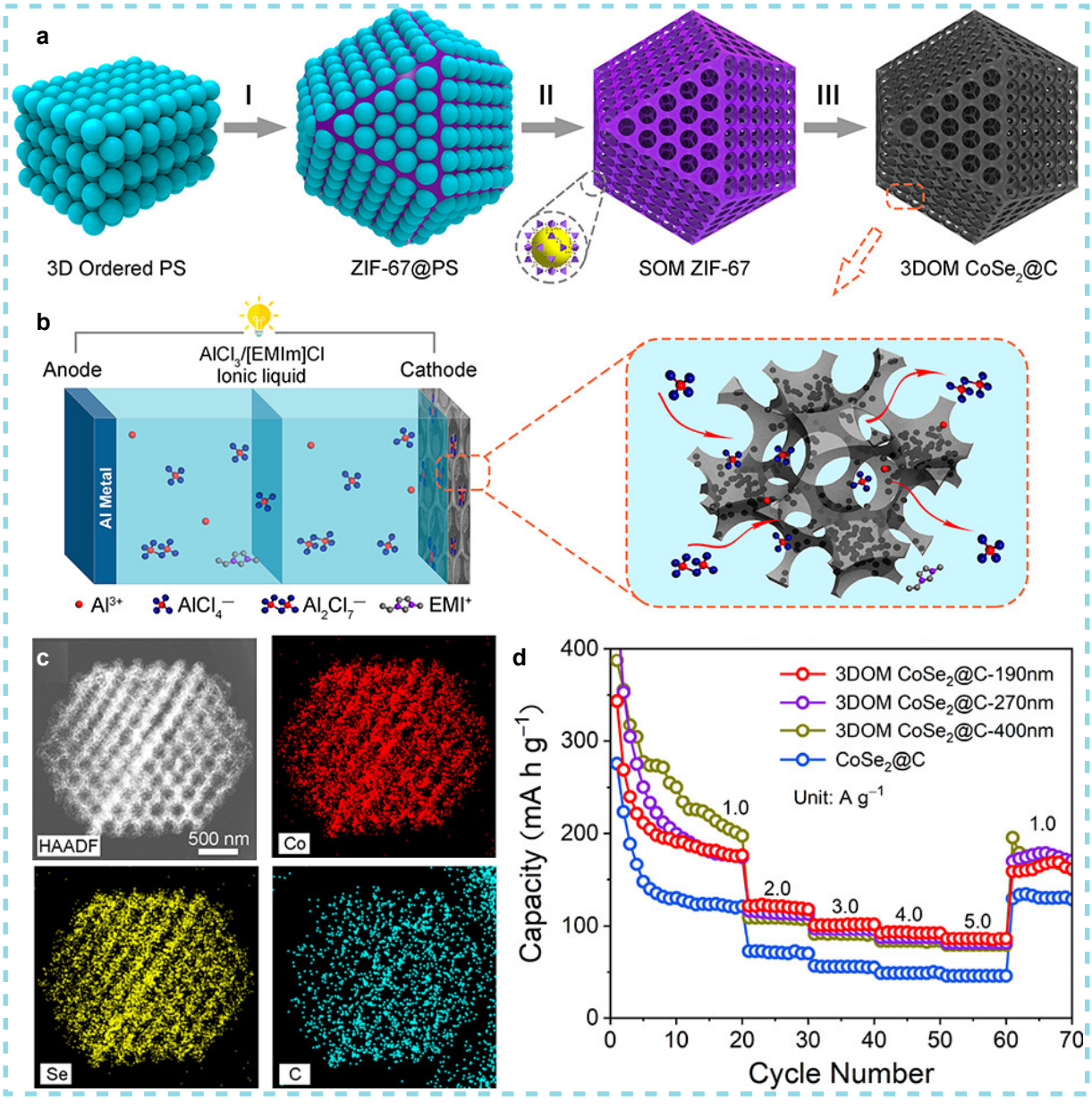

Figure 8 (a) Synthesis of 3DOM $CoSe_2$@C. (b) Schematic of the working mechanism of rechargeable Al/3DOM $CoSe_2$@C cell, illustrating the diffusion of large-sized $Al_xCl_y^-$ and the electrolyte inside the interconnected macroporous network. (c) HAADF-STEM image and corresponding energy dispersive X-ray elemental mappings of Co, Se, C, and N. (d) Rate performance of 3DOM $CoSe_2$@C and $CoSe_2$@C at various current densities. Reproduced with permission from Ref. [54] ©2019, American Chemical Society.

with a coulombic efficiency of approximately 98% and retained a capacity of 35.6 mAh g^{-1} after 1000 cycles at 1 A g^{-1} (Fig. 9b). Beyond the utilization of 3D MOF architectures, Guo et al.[56] synthesized 2D MOFs via a hydrothermal method and further fabricated composite cathode materials by combining these 2D MOFs with GO (Figs. 9c and 9d). Among the synthesized composites, the 2D Cu-based MOFs@rGO composite with 5% rGO exhibited the optimal electrochemical performance, delivering a reversible capacity of 184 mAh g^{-1} at 50 mA g^{-1}, surpassing that of most conventional cathodes for nonaqueous AIBs. Moreover, the composite maintained a stable capacity of 155 mAh g^{-1} after 1000 cycles at 200 mA g^{-1} (Fig. 9e). As shown in Fig. 9f, when the scan rate was increased from 0.2 to 1.0 mV s^{-1}, the intensity of the current related to the redox peaks gradually increased, indicating relatively ideal electrochemical reversibility and reaction kinetics. The authors also investigated the mechanism of the electrochemical reaction in depth, as illustrated in Fig. 9g, demonstrating three consecutive steps: ligand oxidation, ligand reduction, and Cu node reduction. In general, the low conductivity of MOFs, which curtails their use as cathodes for nonaqueous AIBs, has been resolved, achieving high energy density. However, the aluminum-storage mechanism remains unclear, and the cycling stability of these materials is poor.

In addition to MOFs, COFs have also been employed as cathodes for nonaqueous AIBs[64]. Peng et al.[57] prepared a carbonyl-rich DAQ-TpO COF by constructing diaminoanthraquinone (DAQ) and triformylphloroglucinol (TpO) units on carbon nanotubes. This was the first application of COFs as cathodes for nonaqueous AIBs (Fig. 10a). The

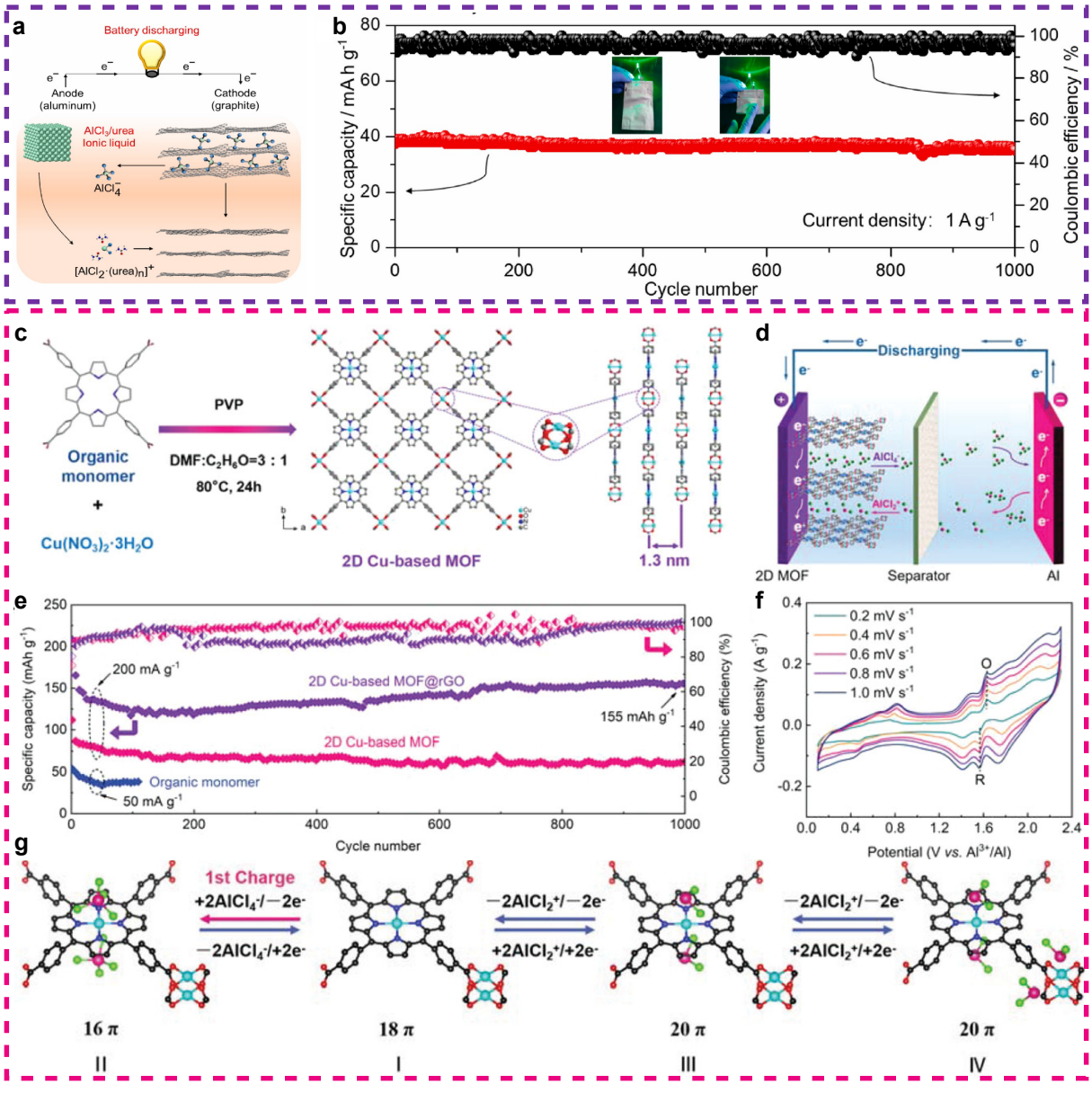

Figure 9 (a) Mechanism of electrochemical reaction in hierarchical porous carbon octahedrons. (b) Long-cycle performance of HPCO. Reproduced with permission from Ref. [55] ©2022, Elsevier Ltd. (c, d) Schematic of energy-storage mechanism in 2D Cu-based MOFs. (e) Cycling performance of organic monomer, 2D Cu-based MOF, and 2D Cu-based MOF@rGO electrodes at 200 mA g^{-1}. (f) CV curves of 2D Cu-based MOF@rGO electrode at different scan rates. (g) Schematic of mechanism of electrochemical reaction in 2D Cu-based MOFs. Reproduced with permission from Ref. [56] ©2022, Wiley-VCH GmbH.

material remained stable for 32,000 charge–discharge cycles at a high-current density of 10 A g^{-1} while still retaining a reversible capacity of 170 mAh g^{-1} and maintaining a coulombic efficiency of 100% (Fig. 10b). Their studies confirmed that $AlCl_2^+$ acts as the primary charge carrier for aluminum storage, and further identified the C=O and C–N groups as the core active sites for $AlCl_2^+$ immobilization (Fig. 10c). Furthermore, Wei et al.[40] synthesized a triphenylamine (TPA)-based COF for AIBs cathodes using TPA as the building block (Fig. 10d). The charge–discharge curves are compared in Fig. 10e, where the TPA-COF features a stable charge–discharge plateau and significantly higher capacity than the reference materials. The AIBs employing this cathode delivered a capacity retention of 84.8% after 3,000 cycles at 1 A g^{-1}, with nearly 100% coulombic efficiency (Fig. 10f). It overcomes the inherent drawbacks of organic cathode materials, namely, the dissolution of small-molecule organics and agglomeration of macromolecular organics. Through DFT simulations and various ex situ characterizations, they also elucidated that the C–N and C=N groups in TPA-COF serve as reversible active sites for $AlCl_2^+$ storage. COF-based materials exhibit exceptional electrochemical performance when used as cathodes for nonaqueous AIBs, but their prohibitively high synthesis cost has greatly limited their practical applicability and large-scale deployment.

In summary, the unique structural advantages of MOF- and COF-derived materials offer broad prospects for the development of cathode materials for nonaqueous AIBs. Through meticulous design of the precursors and pyroly-

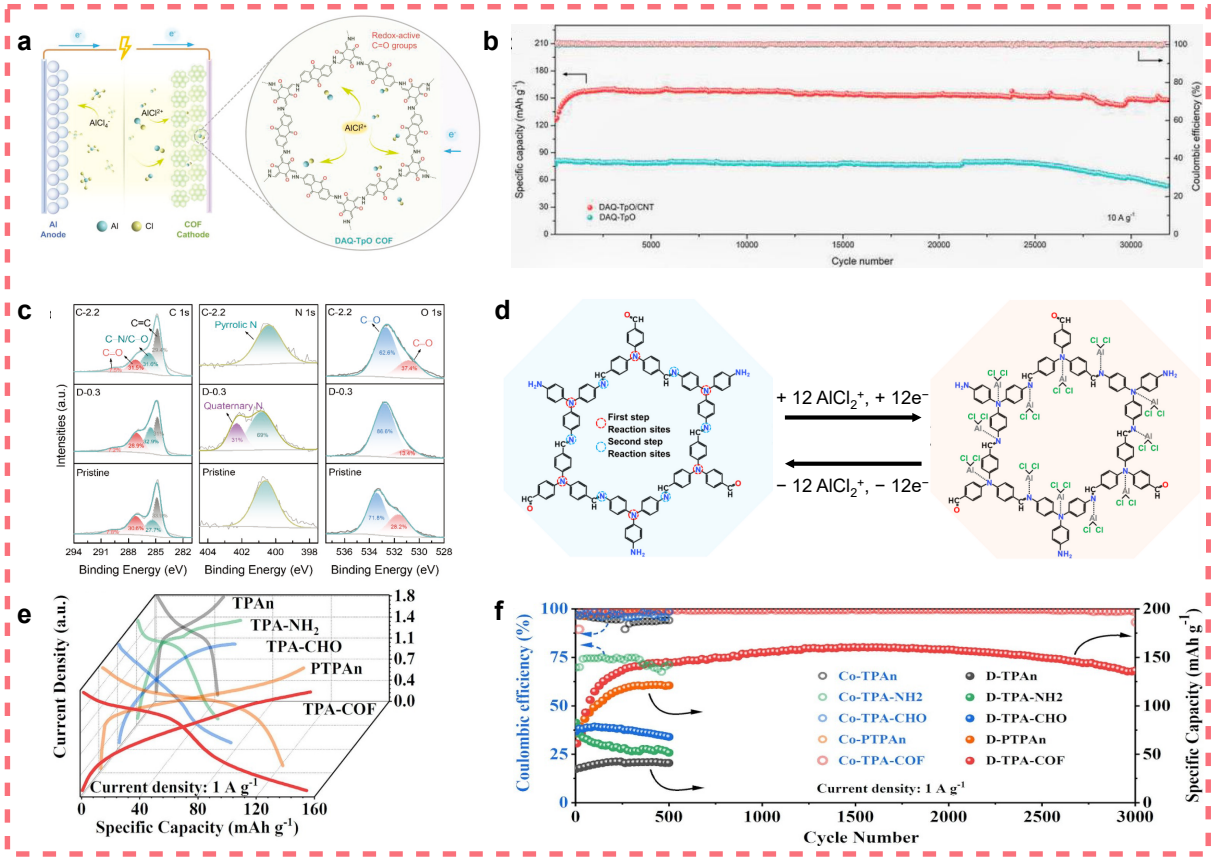

Figure 10 (a) Schematic of Al-organic battery featuring carbonyl-rich DAQ-TpO COF as the cathode and Al metal as the anode in an electrolyte comprising $AlCl_3$/[EMIm]Cl. (b) Cycling performance of DAQ-TpO/CNT and DAQ-TpO at 10 A g^{-1}. (c) High-resolution X-ray photoelectron spectroscopy profiles of C 1s, N 1s, and O 1s regions for the pristine, discharged (D-0.3), and charged (C-2.2) electrodes. Reproduced under the CC-BY-NC license from Ref. [57] ©2024, The Authors. (d) Schematic of charge–discharge mechanism in TPA-COFs for nonaqueous AIBs. (e) Charge–discharge curves at a current density of 1 A g^{-1} in the voltage range of 0.1–1.8 V. (f) Long-term cycling performance at a current density of 1 A g^{-1} in the voltage range of 0.1–2.4 V. Reproduced with permission from Ref. [40] ©2025, Elsevier B.V.

sis/post-treatment processes, porous carbon, metal oxide/sulfide/selenide composites, or single-atom catalysts can be prepared, effectively alleviating volume strain, promoting ion/electron transport, and enhancing the interaction with aluminum chloride complexes through surface modification or heteroatom doping, thereby improving the specific capacity, cycling stability, and reaction kinetics of nonaqueous AIBs. Despite persistent challenges in regulating the conductivity, achieving large-scale preparation, and understanding the long-term cycling mechanisms, MOF/COF-derived materials exhibit structural flexibility and tunable functions, which can be exploited in the future design of high-performance and low-cost cathode materials for nonaqueous AIBs.

2.6 Other cathode materials

Research related to cathode materials for nonaqueous AIBs has made significant progress in recent years. Moreover, the five major types of materials, as well as emerging materials such as MXene, sulfur, and tellurium, have also demonstrated great application potential. MXene, a 2D transition-metal carbide/nitride derived from MAX phase precursors, has excellent potential as a cathode material for energy storage in nonaqueous AIBs owing to its layered structure, high metallic conductivity, and unique surface chemical properties. Li et al.[65] obtained Ti_3C_2 MXene through selective etching with hydrofluoric acid solution, increased its interlayer spacing using cetyltrimethylammonium bromide (CTAB), and finally selenized it to produce Ti_3C_2@CTAB-Se with a two-dimensional, layered structure. Because of its large interlayer structure and high conductivity, Ti_3C_2@CTAB-Se is highly favorable for the intercalation/deintercalation of Al^{3+}, affording enhanced ion diffusion and electron transport capabilities, and effectively inhibiting dissolution of the active material Se and the curtailment of electrochemical reactions caused by the shuttle effect.

Sulfur, as a cathode material, has a comparatively high theoretical specific capacity as it possesses no metal elements, and is thus considered a highly promising material. Aluminum–sulfur batteries have a moderate voltage of 1.25 V, high power density, and an energy density of up to 1340 Wh kg^{-1}, which is more than three times that of commercial lithium–cobalt-oxide–graphite batteries.

Although sulfur and selenium suffer from issues such as low electrical conductivity and volume expansion, the electrical conductivity of tellurium far exceeds that of sulfur and selenium (2×10^4 S m^{-1}) and tellurium has a higher theoretical specific capacity (1260 mAh g^{-1}). However, the reduction of the active material in tellurium electrodes

owing to the shuttle effect, the precipitation of soluble tellurides at the anode, anode corrosion, and a decline in battery capacity are persistent problems. To address these issues, Zhang et al.[66] used nitrogen-doped porous carbon (N-PC) derived from MOFs as the carrier for Te nanowires, combined with modification using polydiallyldimethylammonium chloride and rGO encapsulation, to effectively protect the active material and suppress the shuttle effect, resulting in an initial specific capacity of 935.5 mAh g^{-1} for the N-PC-rGO-Te cathode at 500 mA g^{-1}, and the retention of 467 mAh g^{-1} after 150 cycles.

3 Conclusion and perspective

This review summarizes progress in research on cathode materials for nonaqueous AIBs, focusing on the long-standing issues of low capacity and poor cycling performance. It elaborates on the mechanisms of action of various cathode types, including carbon-based cathodes, transition-metal sulfide and oxide cathodes, organic cathodes, heterojunction cathodes, MOFs/COFs and their derivative cathodes, MXene, and sulfur and tellurium. The significant roles of these materials in enhancing the specific capacity, cycling life, and rate performance of nonaqueous AIBs are also discussed. Despite the theoretical potential of nonaqueous AIBs, cathode materials for nonaqueous AIBs face unresolved problems. Primarily, the intercalation of bulky chloroaluminate complexes (e.g., $[AlCl_4]^-$) into host frameworks induces massive volume expansion and significant mechanical strain, eventually leading to structural pulverization and exfoliation of the active material. Furthermore, the strong coulombic repulsion between the high-charge-density aluminum species and the host lattice creates high barriers for ion migration, resulting in sluggish diffusion kinetics and a drastic reduction in the specific capacity under high-current regimes. Crucially, the electrochemical instability at the cathode/electrolyte interface remains a critical concern; parasitic side-reactions and the oxidative decomposition of ionic-liquid electrolytes at high potentials trigger the formation of high-impedance resistive layers, leading to irreversible capacity loss and compromised cycling longevity. Moreover, there is a lack of relevant theoretical research. Based on the above analysis, we propose the following possible future research directions for the cathodes of nonaqueous AIBs (Fig. 11).

(1) Constructing multifunctional composite materials. Single materials cannot effectively meet the requirements for active sites, structural stability, rapid ion/electron transport, sustainability, and low cost in high-performance batteries. Therefore, multicomponent and multi-structural composite electrodes should be rationally designed to leverage synergistic effects among components and achieve high-performance nonaqueous AIBs (e.g., by combining tellurium/carbon nanotubes and Te nanowires with MOF derivatives).

(2) Reduce or avoid the use of binders and conductive agents. To increase the energy density and specific capacity of batteries, advanced cathode materials (e.g., GA films) or effective designs should be developed to reduce or eliminate the use of binders and conductive agents, thereby increasing the proportion of active materials in the elec-

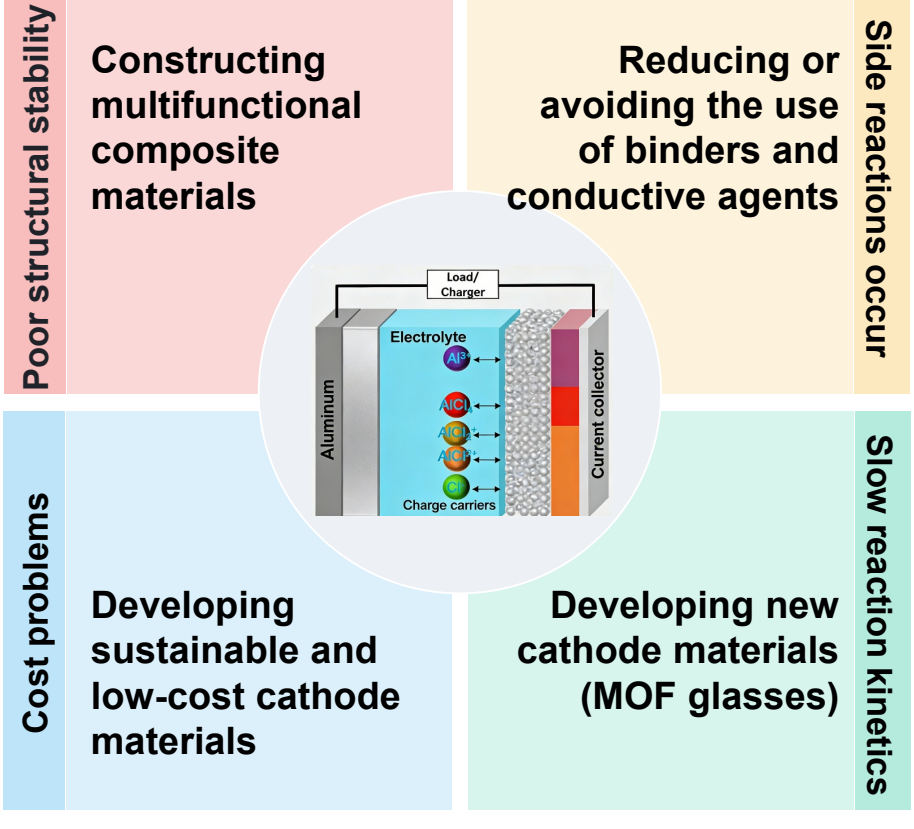

Figure 11 Schematic of challenges and prospective strategies for advancing cathode materials for nonaqueous AIBs.

trode and effectively suppressing possible side-reactions during charging and discharging.

(3) Developing sustainable and low-cost cathode materials. Considering the low cost and abundance of aluminum, the key to the commercialization of nonaqueous AIBs lies in the sustainability and low cost of the cathode materials. Future large-scale energy storage requires high-abundance, sustainable cathode-material resources, primarily the abundant elements in the Earth's crust. By reducing raw material costs and simplifying the preparation process, low-cost, high-yield strategies for synthesizing cathode materials for nonaqueous AIBs can be developed.

(4) Developing new cathode materials. MOF glasses are gradually earning recognition as highly promising cathode candidates for nonaqueous AIBs owing to the advantageous high porosity and structural tunability of MOFs, as well as the amorphous structure, good interface compatibility, and corrosion resistance of the glass materials. Rational design of the composition and structure of MOF glasses is expected to enable a synergistic improvement in the aluminum-ion storage, cycling stability, and reaction kinetics, thereby achieving nonaqueous AIBs with high energy density, long life, and safety.

Acknowledgements

Panpan Dong would like to acknowledge the support from Sichuan Science and Technology Program, Start-up Research Funding of Southwest Jiaotong University, the Fundamental Research Funds for the Central Universities, and Postdoctoral Fellowship Program of China Postdoctoral Science Foundation.

Author contribution statement

Liangjie Gu: Investigation, Writing-original draft. Ming Lei: Investigation, Writing-review & editing. Panpan Dong: Investigation, Supervision, Writing-review & editing. All the authors have approved the final manuscript.

Data availability

Not applicable.

Declaration of competing interest

Panpan Dong is the guest editor of the current special issue, but she was not involved in the peer review or decision of this article. All the other contributing authors report no conflicts of interest in this work.

Funding

This work is granted by Sichuan Science and Technology Program (Grant No. 2025ZNSFSC1413), Start-up Research Funding of Southwest Jiaotong University (Grant No. 2682024KJ003), the Fundamental Research Funds for the Central Universities (Grant No. 2682024CX059), and Postdoctoral Fellowship Program of China Postdoctoral Science Foundation (Grant No. GZC20241407).

Use of AI statement

None.

References

[1] Liang, F., Wang, S. Z., Liang, Q., Zhong, A., Yang, C., Qian, J., Song, H. J., Chen, R. J. (2024). Insight into all-solid-state Li–S batteries: challenges, advances, and engineering design. *Adv. Energy Mater.* 14, 2401959.

[2] Xie, Y. F., Xu, L. L., Tong, Y., Ouyang, Y., Zeng, Q. H., Li, D. X., Xiao, Y. B., Yu, S. T., Liu, X. L., Zheng, C., et al. (2024). Molten guest-mediated metal–organic frameworks featuring multi-modal supramolecular interaction sites for flame-retardant superionic conductor in all-solid-state batteries. *Adv. Mater.* 36, 2401284.

[3] Huang, Y. M., Li, J. (2022). Key challenges for grid-scale lithium-ion battery energy storage. *Adv. Energy Mater.* 12, 2202197.

[4] Feng, X. N., Ren, D. S., Ouyang, M. G. (2023). Safety of lithium battery materials chemistry. *J. Mater. Chem. A* 11, 25236–25246.

[5] Chen, Y. Q., Yan, S. M., Chen, L., Zhao, D., Ding, Y., Zeng, Y. B., Chen, Z. X. (2025). Recent advances in fast‐charging sodium‐ion batteries. *Small* 21, 2412681.

[6] Li, Q., Ulissi, U., Liang, Z. B., Chen, X. X., Guo, B. K., Zhang, X. X., Ouyang, C. Y. (2026). Progress and prospect of industrialization of sodium-ion battery in China. *Adv. Energy Mater.* 16, e04877.

[7] Ramesh, A., Tripathi, A., Balaya, P. (2022). A mini review on cathode materials for sodium-ion batteries. *Int. J. Appl. Ceram. Technol.* 19, 913–923.

[8] Mizanuzzaman, M., Chowdhury, M. A., Khandaker, T., Islam, M. S., Kowser, M. A., Islam, M. M. (2025). Advancements in cathode materials for high-performance rechargeable magnesium-ion batteries. *J. Energy Storage* 118, 116213.

[9] Wang, G. X., Wang, Z. C., Shi, H. C., Du, A. B., Sun, M. L., Cui, G. L. (2024). Progress and perspective on rechargeable magnesium-ion batteries. *Sci. China Chem.* 67, 214–246.

[10] Li, M. N., Wang, C. Y., Wang, C., Lyu, Y., Wang, J. X., Xia, S. X., Mao, J. F., Guo, Z. P. (2025). 10 years development of potassium-ion batteries. *Adv. Mater.* 37, 2416717.

[11] Dhir, S., Jagger, B., Maguire, A., Pasta, M. (2023). Fundamental investigations on the ionic transport and thermodynamic properties of non-aqueous potassium-ion electrolytes. *Nat. Commun.* 14, 3833.

[12] Xue, R., Zhang, R., Liu, Y. S., Guo, J. X. (2025). Multifunctional covalent organic frameworks for zinc-ion batteries. *Coord. Chem. Rev.* 544, 216987.

[13] Wu, Z. X., Li, Q., Chen, Z., Zhi, C. Y. (2025). Calendar aging of zinc-ion batteries. *Matter* 8, 102137.

[14] Li, C. X., Hou, C. C., Chen, L. Y., Kaskel, S., Xu, Q. (2021). Rechargeable Al-ion batteries. *EnergyChem* 3, 100049.

[15] Elia, G. A., Kravchyk, K. V., Kovalenko, M. V., Chacón, J., Holland, A., Wills, R. G. A. (2021). An overview and prospective on Al and Al-ion battery technologies. *J. Power Sources* 481, 228870.

[16] Yu, H. M., Zhang, X. F., Wang, Y. X., Li, M. L., Chen, W., Hu, Z., Zhu, M. S., Huang, Y. (2025). Activation and stabilization strategies of aluminum metal anode toward high performance aqueous al metal batteries. *Adv. Mater.* 37, 2507164.

[17] Yu, H. M., Lv, C. D., Yan, C. S., Yu, G. H. (2024). Interface engineering for aqueous aluminum metal batteries: current progresses and future prospects. *Small Methods* 8, 2300758.

[18] Meng, J. S., Zhu, L. J., Haruna, A. B., Ozoemena, K. I., Pang, Q. Q. (2021). Charge storage mechanisms of cathode materials in rechargeable aluminum batteries. *Sci. China Chem.* 64, 1888–1907.

[19] Ramasubramanian, B., De, A., Koperski, M., Ramakrishna, S., Chellappan, V. (2025). State-of-the-art carbon cathodes with their intercalation chemistry, performance, and challenges for aluminum-ion batteries. *ACS Appl. Energy Mater.* 8, 683–698.

[20] Shen, X. J., Sun, T., Yang, L., Krasnoslobodtsev, A., Sabirianov, R., Sealy, M., Mei, W. N., Wu, Z. J., Tan, L. (2021). Ultra-fast charging in aluminum-ion batteries: electric double layers on active anode. *Nat. Commun.* 12, 820.

[21] Feng, J. Y., Chen, S. M., Wu, Y. Z., Huang, X. D., Yu, C. Z. (2026). Recent advances and design strategies of cathode materials for aqueous aluminum-ion batteries. *Chem. Sci.* 17, 1932–1963.

[22] Wang, Z. B., Gu, H. Q., Wu, T. C., Zhang, W. M., Li, Z. Y. (2025). Enhanced dynamics of Al^{3+}/H^{+} ions in aqueous aluminum ion batteries: construction of metastable structures in vanadium pentoxide upon oxygen vacancies. *J. Energy Chem.* 101, 562–569.

[23] Hu, Y. H., Li, H. L., Gu, H. Q., Li, W., Zhang, M. Y., Zhang, W. J., Zheng, W. H., Li, Z. Y. (2025). Anion redox-driven engineering of layered MnO_2 cathodes for high-capacity aqueous Al-ion batteries. *Chem. Eng. J.* 524, 168881.

[24] Chen, S. M., Gadelhak, N. A., Wu, Y. Z., Feng, J. Y., Yu, C. Z., Huang, X. D., Nanjundan, A. K. (2026). Aqueous aluminium-ion batteries: cathode material design, anode engineering and electrolyte innovation. *Small* 22, e07888.

[25] Huang, R., Luo, S. H., Sun, Q., Yan, S. X. (2024). Insights on energy storage mechanism and rational design of chalcogenide-based cathode materials towards advanced non-aqueous Al-ion batteries. *J. Energy Storage* 93, 112384.

[26] Wei, T. T., Peng, P. P., Qi, S. Y., Zhu, Y. R., Yi, T. F. (2021). Advancement of technology towards high-performance non-aqueous aluminum-ion batteries. *J. Energy Chem.* 57, 169–188.

[27] Pan, W. D., Liu, C., Wang, M. Y., Zhang, Z. J., Yan, X. Y., Yang, S. C., Liu, X. H., Wang, Y. F., Leung, D. Y. C. (2022). Non-aqueous Al-ion batteries: cathode materials and corresponding underlying ion storage mechanisms. *Rare Met.* 41, 762–774.

[28] Nandi, S., Pumera, M. (2024). Transition metal dichalcogenide-based materials for rechargeable aluminum-ion batteries: a mini-review. *ChemSusChem* 17, e202301434.

[29] Guo, Y. Q., Lim, G. J. H., Verma, V., Cai, Y., Chua, R., Lim, J. J. N., Srinivasan, M. (2023). Solid state zinc and aluminum ion batteries: challenges and opportunities. *ChemSusChem* 18, e202202297.

[30] Huang, Z., Song, W. L., Liu, Y. J., Wang, W., Wang, M. Y., Ge, J. B., Jiao, H. D., Jiao, S. Q. (2022). Stable quasi-solid-state aluminum batteries. *Adv. Mater.* 34, 2104557.

[31] Lin, M. C., Gong, M., Lu, B. G., Wu, Y. P., Wang, D. Y., Guan, M. Y., Angell, M., Chen, C. X., Yang, J., Hwang, B. J., et al. (2015). An ultrafast rechargeable aluminium-ion battery. *Nature* 520, 324–328.

[32] Yu, Z. J., Kang, Z. P., Hu, Z. Q., Lu, J. H., Zhou, Z. G., Jiao, S. Q. (2016). Hexagonal NiS nanobelts as advanced cathode materials for rechargeable Al-ion batteries. *Chem. Commun.* 52, 10427–10430.

[33] Wang, S., Yu, Z. J., Tu, J. G., Wang, J. X., Tian, D. H., Liu, Y. J., Jiao, S. J. (2016). A novel aluminum-ion battery: Al/$AlCl_3$-[EMIm]Cl/Ni_3S_2@graphene. *Adv. Energy Mater.* 6, 1600137.

[34] Yang, H. C., Yin, L. C., Liang, J., Sun, Z. H., Wang, Y. Z., Li, H. C., He, K., Ma, L. P., Peng, Z. Q., Qiu, S. Y., et al. (2018). An aluminum–sulfur battery with a fast kinetic response. *Angew. Chem. Int. Ed.* 57, 1898–1902.

[35] Cai, T. H., Zhao, L. M., Hu, H. Y., Li, T. G., Li, X. C., Guo, S., Li, Y. P., Xue, Q. Z., Xing, W., Yan, Z. F., et al. (2018). Stable $CoSe_2$/carbon nanodice@reduced graphene oxide composites for high-performance rechargeable aluminum-ion batteries. *Energy Environ. Sci.* 11, 2341–2347.

[36] Li, C. X., Dong, S. H., Wang, P., Wang, C. X., Yin, L. W. (2019). Metal-organic frameworks-derived tunnel structured $Co_3(PO_4)_2$@C as cathode for new generation high-performance Al-ion batteries. *Adv. Energy Mater.* 9, 1902352.

[37] Li, Z. Y., Lv, W. R., Wu, G. H., Zhang, W. M. (2022). Hollow nanotubes carbon@tellurium for high-performance Al-Te batteries. *Electrochim. Acta* 401, 139498.

[38] Zhang, C., Gu, H. Q., Hu, Y. H., Zhang, W. M., Li, Z. Y. (2023). Investigation on the energy storage performance of Cu_2Se@MnSe heterojunction hollow spherical shell for aluminum-ion battery. *Chem. Eng. J.* 474, 145688.

[39] Wang, D. D., Zhao, L. M., Cui, Y. P., Tong, Y. F., Li, X. J., Liu, P. Y., Hu, H. Y., Nan, J., Wu, W., Xu, H., et al. (2024). Intermolecular π-π stacking of oligomeric naphthalene cathodes facilitate high performance aluminum ion battery. *Chem. Eng. J.* 482, 148806.

[40] Wei, G. K., Qiao, J., Li, X., Dou, A. C., Hu, S. J., Xie, W., Luo, Z. H., Yang, J. H. (2025). High performance rechargeable aluminium ion batteries enabled by strategy of covalent organic frame material. *Chem. Eng. J.* 511, 161845.

[41] Ghasemiahangarani, P., Farhan, G., del Mundo, D., Schoetz, T. (2025). Charge storage mechanisms in batteries and capacitors: a perspective of the electrochemical interface. *Adv. Energy Mater.* 15, 2404704.

[42] Wang, L., Qiu, J. C., Feng, J. M., Dong, L., Long, C. L., Li, D. J., Wang, X. W. (2024). Graphite nanosheets exfoliated by supercritical carbon dioxide for aluminium-ion battery. *Surf. Innov.* 12, 417–428.

[43] Zhang, D., Wang, Z. S., Bao, X. Y., Hong, R. Y., Zhang, X., Xu, J. J. (2024). A green and low-cost approach to recover graphite for high-performance aluminum ion battery cathode. *Mater. Today Sustain.* 28, 100957.

[44] Xue, S., Li, K., Lin, Z., Zhang, K., Zheng, J., Zhang, M., Shen, Z. (2022). Rechargeable aluminum-ion battery based on interface energy storage in two-dimensional layered graphene/TiO_2 electrode. *Mater. Today Sustain.* 20, 100213.

[45] Xing, W., Li, X. C., Cai, T. H., Zhang, Y., Bai, P., Xu, J., Hu, H., Wu, M. B., Xue, Q. Z., Zhao, Y., et al. (2020). Layered double hydroxides derived NiCo-sulfide as a cathode material for aluminum ion batteries. *Electrochim. Acta* 344, 136174.

[46] Li, T. G., Cai, T. H., Hu, H. Y., Li, X. J., Wang, D. D., Zhang, Y., Cui, Y. P., Zhao, L. M., Xing, W., Yan, Z. F. (2022). Multivalent cationic and anionic mixed redox of an Sb_2S_3 cathode toward high-capacity aluminum ion batteries. *J. Mater. Chem. A* 10, 10829–10836.

[47] Xing, L. L., Owusu, K. A., Liu, X. Y., Meng, J. S., Wang, K., An, Q. Y., Mai, L. (2021). Insights into the storage mechanism of VS_4 nanowire clusters in aluminum-ion battery. *Nano Energy* 79, 105384.

[48] Mahar, N., Saleh, T. A., Al-Ahmed, A., Al-Saadi, A. A. (2025). High performance, low-cost rechargeable aluminum ion battery using Nb_2CT_x-MoS_2 composite cathode. *Energy Mater.* 5, 500049.

[49] Ming, L. C., Qiao, J., Wei, G. K., Li, X., Yang, J. H., Tang, Z. C., Liu, Y. Y. (2025). Binder-free FeS_2@CNT self-supported film as cathode for chloride molten salt aluminium batteries. *J. Electrochem. Soc.* 172, 100508.

[50] Wang, Y., Cai, J. F., Han, T. L., Hu, C. Q., Zhu, Y. J., Li, J. J., Liu, J. Y. (2022). *In-situ* growing polyaniline nano-spine array on $FeVO_4$ nanobelts as high-performance rechargeable aluminum-ion battery cathode. *Appl. Surf. Sci.* 591, 153157.

[51] Li, T. G., Hu, H. Y., Cai, T. H., Liu, X. Q., Zhang, Y., Zhao, L. M., Xing, W., Yan, Z. F. (2022). Ultrafast and long-cycle stable aluminum polyphenylene batteries. *ACS Appl. Mater. Interfaces* 14, 30927–30936.

[52] Zhang, C., Chen, M. J., Zhao, X. H., Zhang, W. M., Li, Z. Y. (2023). High-performance $MnSe_2$-MnSe heterojunction hollow sphere for aluminum ion battery. *J. Colloid Interface Sci.* 652, 1438–1446.

[53] Hu, Y. H., Li, H. L., Zhao, X. H., Zhang, W. M., Li, Z. Y. (2024). Organometallic structure-based β_{CD}@$FeSe_2$/$CoSe_2$ heterostructures cathodes for high-performance aluminum-ion battery. *Scr. Mater.* 244, 116004.

[54] Hong, H., Liu, J. L., Huang, H. W., Etogo, C. A., Yang, X. F., Guan, B. Y., Zhang, L. (2019). Ordered macro-microporous metal-organic framework single crystals and their derivatives for rechargeable aluminum-ion batteries. *J. Am. Chem. Soc.* 141, 14764–14771.

[55] Wang, L., Zhu, G. Y., Lin, Y. H., Wang, Y., Zhu, Q. S., Dai, Z. H. (2023). MOF-derived hierarchical porous carbon octahedrons for aluminum-ion batteries. *Carbon* 202, 305–313.

[56] Guo, Y. X., Wang, W., Lei, H. P., Wang, M. Y., Jiao, S. Q. (2022). Alternate storage of opposite charges in multisites for high-energy-density Al-MOF batteries. *Adv. Mater.* 34, 2110109.

[57] Peng, X. Y., Baktash, A., Alghamdi, N., Rana, M. M., Huang, Y. X., Hu, X. Y., He, C. L., Luo, Z. R., Ning, J., Wang, L. Z., et al. (2024). Boosting aluminum storage in highly stable covalent organic frameworks with abundant accessible carbonyl groups. *Adv. Energy Mater.* 14, 2400147.

[58] Lei, H. P., Jiao, S. Q., Tu, J. G., Song, W. L., Zhang, X. F., Wang, M. Y., Li, S. J., Chen, H. S., Fang, D. N. (2020). Modified separators for rechargeable high-capacity selenium-aluminium batteries. *Chem. Eng. J.* 385, 123452.

[59] Li, J., Luo, W. B., Zhang, Z., Li, F. H., Chao, Z. S., Fan, J. C. (2023). ZnSe/$SnSe_2$ hollow microcubes as cathode for high performance aluminum ion batteries. *J. Colloid Interface Sci.* 639, 124–132.

[60] Dong, P. P., Zhang, X. H., Hiscox, W., Liu, J. J., Zamora, J., Li, X. Y., Su, M. Q., Zhang, Q., Guo, X. F., McCloy, J., et al. (2023). Toward high-performance metal–organic-framework-based quasi-solid-state electrolytes: tunable structures and electrochemical properties. *Adv. Mater.* 35, 2211841.

[61] Duan, S., Qian, L. T., Zheng, Y., Zhu, Y. F., Liu, X., Dong, L., Yan, W., Zhang, J. J. (2024). Mechanisms of the accelerated Li^+ conduction in MOF-based solid-state polymer electrolytes for all-solid-state lithium metal batteries. *Adv. Mater.* 36, 2314120.

[62] He, H. G., Deng, N. P., Wang, X. Y., Gao, L., Tang, C. Q., Wu, E. J., Ren, J. G., Yang, X. B., Feng, N. N., Gao, D. Z., et al. (2025). Design strategies, characterization mechanisms, and applications of MOFs in polymer composite electrolytes for solid-state lithium metal batteries. *Adv. Funct. Mater.* 35, 2421670.

[63] Liu, M. J., Liu, T. F., Xu, J. L., Shao, L. Y., Shi, X. Y., Sun, Z. P. (2025). Metal-organic frameworks based solid-state electrolytes for lithium metal batteries: modifications and future prospects. *Next Energy* 6, 100191.

[64] Jiang, Z. H., Xie, M. K., Ma, Q. Y., Liu, P. D., Yu, H. M. (2026). MOF/COF-integrated strategies for aqueous zinc batteries: recent progress, modification approaches, and future guidelines. *Dalton Trans.* 55, 17–39.

[65] Li, Z. Y., Wang, X. X., Zhang, W. M., Yang, S. P. (2020). Two-dimensional Ti_3C_2@CTAB-Se (MXene) composite cathode material for high-performance rechargeable aluminum batteries. *Chem. Eng. J.* 398, 125679.

[66] Zhang, X. F., Wang, M. Y., Tu, J. G., Jiao, S. Q. (2021). Hierarchical N-doped porous carbon hosts for stabilizing tellurium in promoting Al-Te batteries. *J. Energy Chem.* 57, 378–385.